Physics - All Scholarship   Physics

Winter 1-29-2021

A tissue-engineered human trabecular meshwork hydrogel for advanced glaucoma disease modeling

Haiyan Li
SUNY Upstate Medical University, Syracuse University

Tyler Bagué
SUNY Upstate Medical University

Alexander Kirschner
SUNY Upstate Medical University

Ana N. Strat
SUNY Upstate Medical University

Haven Roberts
Duke University

See next page for additional authors

Recommended Citation

Author(s)/Creator(s)

Haiyan Li, Tyler Bagué, Alexander Kirschner, Ana N. Strat, Haven Roberts, Robert W. Weisenthal, Alison E. Patteson, Nasim Annabi, W. Daniel Stamer, Preethi S. Ganapathy, and Samuel Herberg

A tissue-engineered human trabecular meshwork hydrogel for advanced glaucoma disease modeling

Haiyan Li [a,b,c], Tyler Bagué [a], Alexander Kirschner [a], Ana N. Strat [a], Haven Roberts [d], Robert W. Weisenthal [a], Alison E. Patteson [c,e], Nasim Annabi [f], W. Daniel Stamer [d], Preethi S. Ganapathy [a,c,g], Samuel Herberg [a,b,c,h,i,*]

[a] Department of Ophthalmology and Visual Sciences, SUNY Upstate Medical University, Syracuse, NY, 13210, USA
[b] Department of Cell and Developmental Biology, SUNY Upstate Medical University, Syracuse, NY, 13210, USA
[c] BioInspired Institute, Syracuse University, Syracuse, NY, 13244, USA
[d] Duke Eye Center, Duke University, Durham, NC, 27708, USA
[e] Department of Physics, Syracuse University, Syracuse, NY, 13244, USA
[f] Department of Chemical and Biomolecular Engineering, University of California Los Angeles, Los Angeles, CA, 90095, USA
[g] Department of Neuroscience and Physiology, SUNY Upstate Medical University, Syracuse, NY, 13210, USA
[h] Department of Biochemistry and Molecular Biology, SUNY Upstate Medical University, Syracuse, NY, 13210, USA
[i] Department of Biomedical and Chemical Engineering, Syracuse University, Syracuse, NY, 13244, USA

ARTICLE INFO

ABSTRACT

Abnormal human trabecular meshwork (HTM) cell function and extracellular matrix (ECM) remodeling contribute to HTM stiffening in primary open-angle glaucoma (POAG). Most current cellular HTM model systems do not sufficiently replicate the complex native three dimensional (3D) cell-ECM interface, limiting their use for investigating POAG pathology. Tissue-engineered hydrogels are ideally positioned to overcome shortcomings of current models. Here, we report a novel biomimetic HTM hydrogel and test its utility as a POAG disease model. HTM hydrogels were engineered by mixing normal donor-derived HTM cells with collagen type I, elastin-like polypeptide and hyaluronic acid, each containing photoactive functional groups, followed by UV crosslinking. Glaucomatous conditions were induced with dexamethasone (DEX), and effects of the Rho-associated kinase (ROCK) inhibitor Y27632 on cytoskeletal organization and tissue-level function, contingent on HTM cell-ECM interactions, were assessed. DEX exposure increased HTM hydrogel contractility, f-actin and alpha smooth muscle actin abundance and rearrangement, ECM remodeling, and fibronectin deposition - all contributing to HTM hydrogel condensation and stiffening consistent with glaucomatous HTM tissue behavior. Y27632 treatment produced precisely the opposite effects and attenuated the DEX-induced pathologic changes, resulting in HTM hydrogel relaxation and softening. For model validation, confirmed glaucomatous HTM (GTM) cells were encapsulated; GTM hydrogels showed increased contractility, fibronectin deposition, and stiffening vs. normal HTM hydrogels despite reduced GTM cell proliferation. We have developed a biomimetic HTM hydrogel model for detailed investigation of 3D cell-ECM interactions under normal and simulated glaucomatous conditions. Its bidirectional responsiveness to pharmacological challenge and rescue suggests promising potential to serve as screening platform for new POAG treatments with focus on HTM biomechanics.

1. Introduction

The human trabecular meshwork (HTM), located in the iridocorneal angle, is an avascular connective tissue with filtering features and complex architecture (Gould and John, 2002). Its main function is to control the resistance to drainage of aqueous humor (AH) via the conventional outflow pathway to maintain normal intraocular pressure (IOP) (Brubaker, 1991). Most of the AH outflow resistance is localized to the deepest juxtacanalicular tissue (JCT) region (Keller and Acott, 2013), where a few discontinuous layers of HTM cells reside in and

interact with a dense amorphous extracellular matrix (ECM). A variety of ECM structural and organizational components have been identified within the JCT; e.g., non-fibrillar and fibrillar collagens, elastic fibrils, and basement membrane-like materials. The narrow space between HTM cells and ECM fibers is filled with a ground substance rich in proteoglycans and the glycosaminoglycan hyaluronic acid (HA) (Abu-Hassan et al., 2014; Acott and Kelley, 2008; Hann and Fautsch, 2011; Keller and Acott, 2013; Tamm, 2009).

HTM cells play an essential role in modulating AH outflow resistance by controlling the production of contraction forces and the secretion/degradation of ECM proteins to support tissue homeostasis (Kelley et al., 2009). As such, the reciprocity between HTM cells and their ECM is critical for normal tissue function and IOP maintenance within narrow margins in the healthy eye. Dysregulation of HTM cells can cause elevated ECM deposition as well as HTM cell and tissue contraction, which jointly contribute to HTM stiffening, ultimately leading to increased AH outflow resistance and elevated IOP (Faralli et al., 2019; Ramos et al., 2009). Prolonged elevation of IOP causes pathologic distension and compression of the HTM and further tissue stiffening. Consequently, the stiffened HTM negatively affects IOP and HTM cell function in a feed-forward loop (Last et al., 2011; Stamer and Acott, 2012; Wang et al., 2017a). Since elevated IOP is a primary risk factor for glaucoma, this pathologic process leads to retinal ganglion cell damage resulting in the irreversible loss of vision that is characterized as primary open-angle glaucoma (POAG), the most common form of glaucoma (Kwon et al., 2009; Quigley, 1993; Quigley and Broman, 2006; Tamm et al., 2015; Tham et al., 2014).

Elevated IOP is the only modifiable risk factor for POAG, and management of the disease is focused on IOP lowering (Kwon et al., 2009). First line POAG medications do not specifically target the diseased HTM; instead, they lower IOP by either increasing AH outflow bypassing the HTM altogether, or by decreasing AH production (Beidoe and Mousa, 2012; Lin et al., 2018). In the United States, only the recently approved Rho-associated kinase (ROCK) inhibitor netarsudil (Serle et al., 2018) directly aims at the stiffened HTM to increase AH outflow via cell/tissue relaxation (Rao et al., 2001, 2017; Tanna and Johnson, 2018; Wang and Chang, 2014; Zhang et al., 2012). However, various adverse events at the ocular surface in some patients have been reported during the drug's brief window of availability (Dasso et al., 2018; Tanna et al., 2020; Wisely et al., 2020), raising concerns over its routine use. This highlights the clear unmet need for new/improved POAG treatment strategies. Targeting ECM mechanics by reversing tissue stiffening to limit pathological progression is an emerging therapeutic approach in other diseases (Lampi and Reinhart-King, 2018), with promising potential for POAG therapy.

A number of models are available to study HTM physiology and POAG pathophysiology; e.g., conventional two dimensional (2D) HTM cell monolayer cultures, perfusion-cultured anterior segments from postmortem human and animal eyes, or animal models of different (large and small) species (Fan et al., 2008; Gerometta et al., 2004; Paylakhi et al., 2012; Rybkin et al., 2017; Stamer et al., 2018). While each of these model systems has proven strengths, they cannot reliably and efficiently determine the relative contributions of HTM cells and their ECM to the onset and progression of glaucomatous HTM stiffening. This has hampered advances in the mechanistic study of this biomechanical element in POAG pathophysiology.

The interdisciplinary field of tissue engineering aims to produce functional biomimetic replicas of tissues of interest (Langer and Vacanti, 1993). HTM tissue engineering is still in its infancy; few studies have been reported that use bioengineered 3D HTM *in vitro* models. Constructs made of porous scaffolds (~20 μm thick) seeded with HTM cells were shown to partially mimic normal *in vivo* tissue function, including pharmacological induction/rescue of glaucomatous conditions (Torrejon et al., 2013, 2016a, 2016b). However, an argument could be made that this model is more akin to a 2D cell culture system (i.e., HTM cells grown on a flat culture substrate) rather than a true 3D model, as it cannot accurately mimic the 3D cell-ECM interface beyond ECM secreted by the HTM cells while grown atop the synthetic polymer scaffold. Another scaffold-based approach utilized porcine TM cells (Osmond et al., 2017) or HTM cells (Osmond et al., 2020) cultured atop a freeze-dried polymer matrix made of collagen and chondroitin sulfate and/or HA exhibiting aligned pores throughout the 3D construct (~3 mm thick). The scaffolds were shown to support TM cell proliferation into the porous matrix, and the bioengineered constructs displayed certain aspects of normal tissue function. Nevertheless, the study did not investigate the constructs' behavior under induced glaucomatous conditions.

In addition to scaffold-based systems, viscoelastic hydrogels (i.e., water-swollen networks of polymers) are widely used in tissue engineering applications. They provide a simplistic version of the natural 3D tissue environment and allow for accurate *in vitro* modeling of cellular behaviors (Green and Elisseeff, 2016; Khademhosseini and Langer, 2007; Lee and Mooney, 2001; Seliktar, 2012; Zhang and Khademhosseini, 2017). To that end, Matrigel, the gelatinous protein mixture secreted by mouse sarcoma cells, has been used to fabricate a rudimentary 3D HTM hydrogel culture model (Bouchemi et al., 2017; Saccà et al., 2020; Vernazza et al., 2019). Significant drawbacks include Matrigel's tumorigenic origin, diverse composition, and batch-to-batch variability affecting its biochemical and mechanical properties (Caliari and Burdick, 2016). Lastly, a recent study reported a shear-thinning peptide hydrogel with HTM cells seeded atop to engineer an injectable HTM implant with utility as *in vitro* model (Waduthanthri et al., 2019). However, this simple 20-residue peptide cannot faithfully recapitulate the complex ECM environment HTM cells interact with in the native tissue. Together, these studies highlight the need for more well-defined hydrogel systems to support relevant HTM modeling studies under normal and induced glaucomatous conditions.

Here, we report a novel tissue-engineered HTM hydrogel composed of normal donor-derived HTM cells and ECM biopolymers found in the native tissue, with focus on modeling the JCT region owing to both its critical role in regulating AH outflow resistance and IOP, and inextricable link to glaucomatous HTM stiffening. HTM hydrogels in different sizes/shapes were formed by mixing HTM cells with collagen type I, HA, and elastin-like polypeptide (ELP) - each containing photoactive functional groups - followed by photoinitiator-mediated short UV cross-linking. We then used proven pharmacological induction of glaucomatous conditions by treating HTM hydrogels with the corticosteroid dexamethasone (DEX) (Rybkin et al., 2017) and assessed the therapeutic effects of the ROCK inhibitor Y27632 (Koga et al., 2006), either as co- or sequential treatment, on cytoskeletal organization and tissue-level functional changes contingent on HTM cell-ECM interactions. To validate our model, we encapsulated glaucomatous HTM (GTM) cells derived from a confirmed POAG donor eye and compared cell proliferation, contractility, fibronectin deposition, and stiffening of GTM hydrogels to normal HTM hydrogels without or with DEX/Y27632 treatment.

2. Materials and methods

2.1. HTM cell isolation and culture

Human donor eye tissue use was approved by the SUNY Upstate Medical University Institutional Review Board (protocol #1211036), and all experiments were performed in accordance with the tenets of the Declaration of Helsinki for the use of human tissue. Normal human trabecular meshwork (HTM) cells were isolated from healthy donor corneal rims discarded after transplant surgery, and cultured according to established protocols (Keller et al., 2018; Stamer et al., 1995). Using an SMZ1270 stereomicroscope (Nikon Instruments, Melville, NY, USA), corneal rims were cut into wedges and the HTM tissue was grabbed by placing one tip of Dumont #5 fine-tipped forceps (Fine Science Tools, Foster City, CA, USA) into the Schlemm's canal lumen and the other on

top of the anterior HTM. The dissected strips of HTM tissue were digested for 20 min with 1 mg/ml collagenase (Worthington, Lakewood, NJ, USA) and 4.5 mg/ml human albumin (Sigma-Aldrich, St. Louis, MO, USA) in Dulbecco's Phosphate Buffered Saline (DPBS; Gibco; Thermo Fisher Scientific, Waltham, MA, USA) at 37 °C, placed into a single well of gelatin-coated (Sigma-Aldrich) 6-well culture plates (Corning; Thermo Fisher Scientific), and overlaid with glass coverslips to aid in tissue adherence. HTM tissue strips were cultured in low-glucose Dulbecco's Modified Eagle's Medium (DMEM; Gibco) containing 20% fetal bovine serum (FBS; Atlanta Biologicals, Flowery Branch, GA, USA) and 1% penicillin/streptomycin/glutamine (PSG; Gibco), and maintained at 37 °C in a humidified atmosphere with 5% CO_2. Fresh media was supplied every 2–3 days. Once confluent, HTM cells were lifted with 0.25% trypsin/0.5 mM EDTA (Gibco) and sub-cultured in DMEM with 10% FBS and 1% PSG. All studies were conducted using cells passage 3–7; the reference HTM cell strain HTM129 was isolated and characterized at Duke University by W.D.S. (Table 1).

2.2. HTM cell characterization

HTM cells were seeded at 1×10^4 cells/cm^2 in 6-well culture plates or on sterilized glass coverslips in 24-well culture plates, and cultured in DMEM with 10% FBS and 1% PSG. HTM cell morphology and growth characteristics were monitored by phase contrast microscopy using an LMI-3000 Series Routine Inverted Microscope (Laxco; Thermo Fisher Scientific). Once confluent, HTM cells were treated with 100 nM dexamethasone (DEX; Fisher Scientific) or vehicle control (0.1% (v/v) ethanol) in DMEM with 1% FBS and 1% PSG for 4 d, and serum- and phenol red-free DMEM for 3 d. The HTM cell culture supernatants were collected and concentrated using Amicon® Ultra Centrifugal Filters (Millipore Sigma, Burlington, MA, USA) for immunoblot analysis. The monolayer HTM cells were processed for quantitative reverse transcription-polymerase chain reaction (qRT-PCR) and immunocytochemistry (ICC) analyses. DEX-induced myocilin (MYOC) upregulation in more than 50% of HTM cells was used as inclusion/exclusion criterion.

2.2.1. Immunoblot analysis

Equal protein amounts (10 μg), determined by standard bicinchoninic acid assay (Pierce; Thermo Fisher Scientific), from concentrated HTM cell culture supernatants ± DEX at 7 d supplemented with Halt™ protease/phosphatase inhibitor cocktail (Thermo Fisher Scientific) in 6X loading buffer (Boston Bio Products, Ashland, MA, USA) with 5% beta-mercaptoethanol (BME; Fisher Scientific) were boiled for 5 min and subjected to SDS-PAGE using NuPAGE™ 4–12% Bis-Tris Gels (Invitrogen; Thermo Fisher Scientific) at 200V for 50 min and transferred to 0.45 μm PVDF membranes (Millipore; Thermo Fisher Scientific). Membranes were blocked with 5% nonfat milk (Nestlé USA, Glendale, CA, USA) in tris-buffered saline with 0.2% Tween®20 (TBST; Thermo Fisher Scientific), and probed with a primary antibody against MYOC (anti-MYOC [MABN866] 1:2000; Sigma-Aldrich) followed by incubation with an HRP-conjugated secondary antibody (Cell Signaling, Danvers, MA, USA). Bound antibodies were visualized with the enhanced chemiluminescent detection system (Pierce) on autoradiography film (Thermo Fisher Scientific).

2.2.2. Quantitative reverse transcription-polymerase chain reaction (qRT-PCR) analysis

Total RNA was extracted from HTM cells ± DEX at 7 d (N = 3 per group and donor) using PureLink RNA Mini Kit (Invitrogen). RNA concentration was determined with a NanoDrop spectrophotometer (Thermo Fisher Scientific). RNA was reverse transcribed using iScript™ cDNA Synthesis Kit (BioRad, Hercules, CA, USA). Fifty nanograms of cDNA were amplified in duplicates in each 40-cycle reaction using a CFX 384 Real Time PCR System (BioRad) with annealing temperature set at 60 °C, Power SYBR™ Green PCR Master Mix (Thermo Fisher Scientific), and custom-designed qRT-PCR primers for MYOC and Glyceraldehyde 3-phosphate dehydrogenase (GAPDH) (IDT, Coralville, IA, USA; Table 2). Transcript levels were normalized to GAPDH, and DEX-induced MYOC mRNA fold-changes calculated relative to vehicle controls using the comparative C_T method (Schmittgen and Livak, 2008).

2.2.3. Immunocytochemistry analysis

HTM cells ± DEX at 7 d were fixed with 4% paraformaldehyde (PFA; Thermo Fisher Scientific) at room temperature for 10 min, permeabilized with 0.5% Triton™ X-100 (Thermo Fisher Scientific), blocked with blocking buffer (BioGeneX, Fremont, CA, USA), and incubated with primary antibodies against MYOC (anti-MYOC [ab41552] 1:200; Abcam, Cambridge, MA, USA) or alpha B-Crystallin (anti-CRYAB [ab13497] 1:200; Abcam) followed by incubation with Alexa Fluor® 488-conjugated secondary antibodies (Abcam). Nuclei were counterstained with 4′,6′-diamidino-2-phenylindole (DAPI; Abcam). Coverslips were mounted with ProLong™ Gold Antifade (Thermo Fisher Scientific) on Superfrost™ Plus microscope slides (Fisher Scientific), and fluorescent images were acquired with an Eclipse N*i* microscope (Nikon). Four fields of view per sample were analyzed to quantify percent of cells expressing MYOC, followed by calculation of mean ± SD as follows: DEX-induced MYOC upregulation = (Mean$_{DEX}$ – Mean$_{Ctrl}$) ± [(SD$_{DEX}$)^2 + (SD$_{Ctrl}$)^2]$^{1/2}$.

2.3. Glaucomatous donor history

Patient was an 81 year old, white female that was taking Brimonidine (1 drop, long-term), Dorzolamide-timolol (22.3–6.8 mg/ml drop), and Latanoprost (0.005% drop) for treatment of ocular hypertension. The patient was diagnosed with moderate stage primary open-angle glaucoma (POAG) in her OS eye, and a high-risk POAG suspect in her OD eye. There was thinning of the nerve fiber layer in the OS eye by optical coherence tomography, which was consistent with Single Field Analysis showing inferior and superior nasal steps. Lastly, the patient's cup to disc ratio, taken by fundus exam in May of 2019, was 0.6 for OD and 0.65 for OS, and both eyes had reached a maximum intraocular pressure of 19 mmHg while under maximal treatment. Upon receipt of donor eyes by W.D.S., outflow facility measurements during constant pressure perfusion conditions were 0.13 and 0.16 μl/min/mmHg from OD and OS eyes, respectively.

2.4. GTM cell characterization

Glaucomatous HTM cells (GTM1445) were isolated from the OD eye of the donor and characterized. GTM cells were seeded at 1×10^6 cells/cm^2 in 6-well culture plates or on sterilized circular glass coverslips (22 mm, non-coated; VWR, Radnor, PA, USA) in 24-well culture plates, and cultured in DMEM with 10% FBS and 1% PSG. Cell morphology and growth were monitored by phase contrast microscopy using an inverted

Table 1
HTM cell strain information.

ID	Sex	Age	Used in
Reference (HTM129)*	Female	75	Fig. 2; Suppl. Fig. S4
HTM01	Female	26	Fig. 2, 3 and 5; Suppl. Fig. S4,5,7
HTM12	Female	60	Fig. 2–8, 10; Suppl. Fig. S4,7,8
HTM19	Male	34	Fig. 2–8; Suppl. Fig. S4,7,8

*obtained from W.D.S. at Duke University.

Table 2
qRT-PCR primer information.

Gene	Forward	Reverse
MYOC	ATTCTTGGGGTGGCTACACG	TGATGAAGGCATTGGCGACT
GAPDH	GTCTCCTCTGACTTCAACAGCG	ACCACCCTGTTGCTGTAGCCAA

light microscope (Zeiss, White Plains, NY, USA). Once confluent, GTM cells were treated with 100 nM DEX (Sigma Life Sciences) or vehicle control (0.1% (v/v) ethanol) in DMEM with 1% FBS and 1% PSG for 7 d.

2.4.1. Immunoblot analysis

GTM1445 cells in 6-well plates were washed with ice-cold 1X DPBS (Gibco, Thermo Fisher Scientific) and lysates were scraped into 2X Laemmli sample buffer (90% sample buffer, 10% BME). Samples were boiled for 5 min, loaded in equal amounts (10 μg) into 10% poly-acrylamide gels (BioRad), and proteins separated using SDS-PAGE at a constant rate of 0.3 amps for 70 min. Proteins in gel slabs were transferred electrophoretically to nitrocellulose membranes (BioRad). Membranes were blocked with 5% nonfat, blotting grade milk (Genesee, San Diego, CA, USA), and probed with a custom primary antibody against MYOC (1:1000 (Stamer et al., 1998)) followed by incubation with an HRP-conjugated goat-anti-rabbit secondary antibody (Jackson Immunoresearch, 1:5000). Bound antibodies were visualized by spraying with HyGLO chemiluminescent HRP antibody detection reagent (Thomas Scientific, Swedesboro, NJ, USA) and visualized using the ChemiDoc Touch Imaging System (BioRad).

2.4.2. Immunocytochemistry analysis

GTM1445 cells on coverslips were washed with ice-cold 1X DPBS, then fixed on ice with 4% PFA (Electron Microscopy Sciences, Hatfield, PA, USA) for 30 min, permeabilized with TX solution (1:1000 Triton® X-100 in DPBS) at room temperature, blocked for 1 h (90% TX solution, 10% goat serum), and incubated with the custom primary antibody against MYOC (1:200) followed by incubation with an Alexa Fluor® 488-conjugated AffiniPure goat-anti-rabbit secondary antibody (1:200; Jackson ImmunoResearch, West Grove, PA, USA). Nuclei were counterstained with DAPI. Coverslips were mounted with Immu-Mount (Shandon; Thermo Scientific) on Premium Frosted microscope slides (Fisher Scientific), and fluorescent images were acquired with an Eclipse 90*i* microscope (Nikon). Three fields of view per sample were analyzed to calculate percent MYOC induction.

2.5. Elastin-like polypeptide (ELP) expression and analysis

A plasmid containing a unique ELP was obtained from N.A. at the University of California, Los Angeles. It consists of 70 repeats of the pentapeptide VPGVG, in which the 1st valine was replaced with isoleucine in every 5th pentapeptide (i.e., ([VPGVG]$_4$[IPGVG]$_{14}$), flanked by KCTS residues to render the ELP UV-crosslinkable (Zhang et al., 2015). The construct was verified by standard nucleotide sequencing using T7 primers (GENEWIZ; South Plainfield, NJ, USA) (Suppl. Fig. S1A). *Escherichia coli (E. coli)* was used as a host to express the protein as described previously (Shirzaei Sani et al., 2018; Zhang et al., 2015). Briefly, a 50 ml E. *coli* starter culture in terrific broth (Thermo Fisher Scientific) was incubated at 37 °C overnight, followed by inoculation (1:100) of the expression culture and incubation at 37 °C for 24 h. Bacterial pellets were collected and resuspended in lysis buffer (10 mM Tris, 1 mM EDTA, 100 mM NaCl, 5 mM MgCl$_2$, 14.3 mM BME; all Thermo Fisher Scientific). Lysozyme (Acros Organics, Fair Lawn, NJ, USA) was added to the solution at 1 mg/ml and samples were incubated for 30 min on ice, followed by 5 min sonication (1 min on, 1 min off). The solution was centrifuged at 15,000 g for 20 min at 4 °C and the supernatant was kept. To precipitate the protein, 1 M NaCl was added and centrifuged at 15,000 g for 20 min at 37 °C. ELP was purified using inverse transition cycling (1 cold spin, 1 hot spin; x3), dialyzed against diH$_2$O at 4 °C for 18 h, and lyophilized. Because ELP precipitates at high temperatures and solubilizes at low temperatures (thermal transition temperature of 29 °C for a 1% (w/v) solution; Suppl. Fig. S1C), these temperature changes provide a way to collect and purify the ELP. To verify the molecular weight of the purified product, ELP was reconstituted in DPBS at 10 mg/ml. Ten micrograms of ELP in 6X loading buffer (Boston Bio Products) with 5% BME (Fisher Scientific) were

subjected to SDS-PAGE using NuPAGE™ 10% Bis-Tris Gels (Invitrogen) at 200V for 40 min. Gels were stained with Coomassie Blue R-250 (Biorad) and de-stained in a solution containing 50% (v/v) diH$_2$O, 40% ethanol, and 10% acetic acid (Sigma-Aldrich). De-stained gels were imaged using a ChemiDoc system (BioRad) (Suppl. Fig. S1).

2.6. Hydrogel precursor solutions

Methacrylate-conjugated bovine collagen type I (MA-COL; molecular weight: ~300 kDa, degree of methacrylation: ~60–70%; Suppl. Fig. S2A; Advanced BioMatrix, Carlsbad, CA, USA) was reconstituted in sterile 20 mM acetic acid at 6 mg/ml. Immediately prior to use, 1 ml MA-COL was neutralized with 85 μl neutralization buffer (Advanced BioMatrix) according to the manufacturer's instructions. Thiol-conjugated hyaluronic acid (SH-HA; Glycosil®; molecular weight: ~300 kDa, degree of thiolation: ~20–30%; Suppl. Fig. S2A; Advanced BioMatrix) was reconstituted in sterile diH$_2$O containing 0.5% (w/v) photoinitiator (4-(2-hydroxyethoxy) phenyl-(2-propyl) ketone; Irgacure® 2959; Sigma-Aldrich) at 10 mg/ml according to the manufacturer's protocol. In-house expressed ELP (SH-ELP; thiol via KCTS flanks; molecular weight: 31.2 kDa, degree of thiolation: bi-functional; Suppl. Fig. S2A) was reconstituted in DPBS at 10 mg/ml and sterilized using a 0.2 μm syringe filter in the cold. These photoactive biopolymers have the ability to form chemical crosslinks via methacrylate, thiol-ester, or disulfide linkages (Suppl. Fig. S2B).

2.7. Preparation of PDMS molds

Custom master molds (8-mm diameter x 1-mm depth, or 8-mm diameter x 2-mm depth) were 3D-printed (F170; Stratasys, Eden Prairie, MN, USA) using ABS-M30 filament (Suppl. Fig. S3). Poly-dimethylsiloxane (PDMS; Sylgard 184, Dow Corning, Midland, MI, USA) was mixed in a 10:1 ratio of elastomer to curing agent according to the manufacturer's protocol, poured into the 3D-printed negative master molds, degassed under vacuum in a desiccator, and cured overnight at 60 °C. The PDMS molds were sterilized under UV light for 30 min prior to use.

2.8. Preparation of HTM hydrogels

HTM or GTM cells (1.0×10^6 cells/ml) were thoroughly mixed with MA-COL (3.6 mg/ml [all final concentrations]), SH-HA (0.5 mg/ml, 0.025% (w/v) photoinitiator), and SH-ELP (2.5 mg/ml) on ice. The HTM/GTM cell-laden hydrogel precursor solution was pipetted: a) onto PDMS-coated (Sylgard 184; Dow Corning) 24-well culture plates (10 μl droplets), b) into custom 8x1-mm PDMS molds (50 μl), c) onto 12-mm round glass coverslips (10 μl droplets) followed by spreading with pipette tips, or d) into standard 24-well culture plates (150 μl) depending on the type of experiment, and UV crosslinked (OmniCure S1500 UV Spot Curing System; Excelitas Technologies, Mississauga, Ontario, Canada) at 320–500 nm, 2.2 W/cm^2 for 1–30 s before transferring constructs to 24-well culture plates (Fig. 1). One milliliter of DMEM with 10% FBS and 1% PSG was added to each well, and constructs were maintained at 37 °C in a humidified atmosphere with 5% CO$_2$. HTM hydrogels were cultured for 1–10 d with media replenished every 3 d. GTM hydrogels were prepared and cultured in the same manner.

2.9. HTM hydrogel microstructural analysis

One hundred microliters of acellular hydrogel precursor solutions were pipetted into custom 8x2-mm PDMS molds, made from 3D-printed templates, UV crosslinked, and equilibrated in DPBS for 3 h to wash off any un-crosslinked polymers. Hydrogel samples were bisected to expose the interior hydrogel network surface and fixed in 4% PFA at 4 °C overnight, washed with DPBS, flash frozen in liquid nitrogen, and
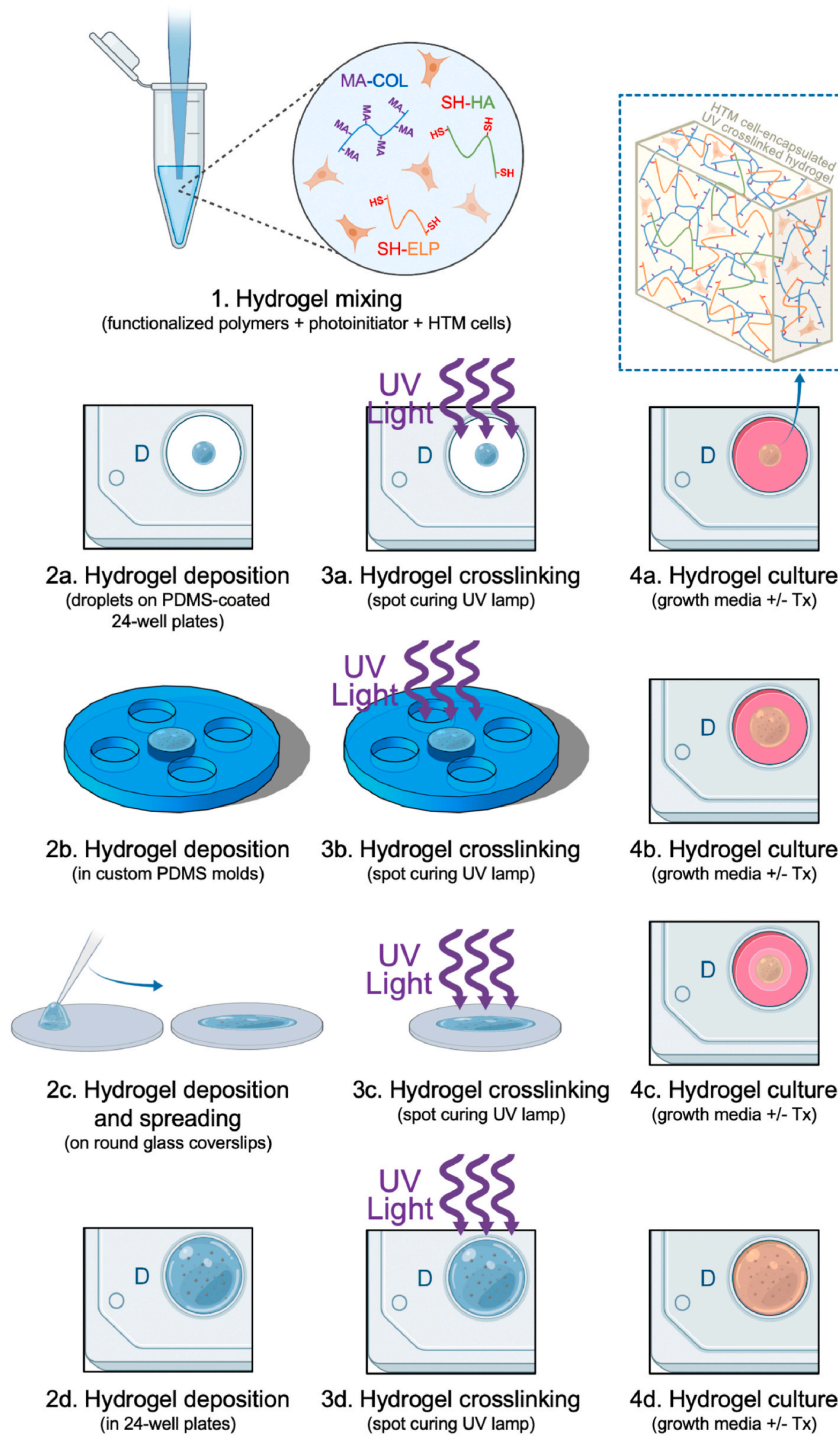
lyophilized. Dried samples were mounted on scanning electron microscopy (SEM) stubs, sputter coated with gold, and visualized using a JSM-IT100 InTouchScope™ SEM (JEOL USA, Peabody, MA, USA) at 7 kV. Two fields of view per sample were analyzed to quantify hydrogel pore size (N = 40 total) using ImageJ software (National Institutes of Health, Bethesda, MD, USA).

2.10. HTM hydrogel cell viability analysis

Cell viability was determined using a LIVE/DEAD™ Viability/Cytotoxicity Kit (i.e., live = green-stained, dead = red-stained) (Invitrogen) according to the manufacturer's instructions. HTM/GTM hydrogels were incubated with the staining solutions (calcein-AM (0.5 μl/ml) and ethidium homodimer-1 (2 μl/ml) in DMEM with 10% FBS and 1% PSG) at 37 °C for 45 min and washed with DPBS. Fluorescent images were

acquired on 0 d (i.e., immediately after UV crosslinking; N = 4 per group and donor) and 7 d (qualitative) with an Eclipse T*i* microscope (Nikon). Four fields of view per sample were analyzed to quantify percent HTM cell viability (i.e., ratio of live to total cells), followed by calculation of mean ± SD.

2.11. HTM hydrogel cell proliferation analysis

Cell proliferation was measured with the CellTiter 96® AQueous Non-Radioactive Cell Proliferation Assay (Promega, Madison, WI, USA) following the manufacturer's protocol. HTM/GTM hydrogels cultured in DMEM with 10% FBS and 1% PSG for 1–10 d (N = 3 per group and donor) were incubated with the staining solution (38 μl MTS, 2 μl PMS solution, 200 μl DMEM) at 37 °C for 1.5 h. Absorbance at 490 nm was recorded using a spectrophotometer plate reader (BioTEK, Winooski, VT, USA). Blank-subtracted absorbance values served as a direct measure of HTM cell proliferation over time.

2.12. HTM hydrogel treatments

HTM hydrogels cultured in DMEM with 10% FBS and 1% PSG were subjected to the following treatments for 10 d: 1) vehicle control (ethanol; 0.1% (v/v)), 2) DEX (100 nM), 3) Rho-associated kinase (ROCK) inhibitor Y27632 (10 μM; Sigma-Aldrich), 4) DEX (100 nM) + Y27632 (10 μM) [co-treatment], or 5) DEX (100 nM) for 5 d followed by Y27632 (10 μM) for 5 d [sequential-treatment]. For comparisons between normal HTM hydrogels and GTM hydrogels, samples were subjected to the following treatments for 7/10 d: 1) vehicle control (ethanol; 0.1% (v/v)), 2) DEX (100 nM), or 3) Y27632 (10 μM).

2.13. HTM hydrogel contraction analysis

HTM/GTM hydrogels were cultured in DMEM with 10% FBS and 1% PSG, in absence or presence of the different treatments (N = 3–4 per group and donor; 3 independent experiments). Longitudinal brightfield images were acquired over 10 d with an Eclipse T*i* microscope (Nikon). Construct area was measured using ImageJ software (NIH) over time and normalized to 0 d.

2.14. HTM hydrogel immunocytochemistry analysis

HTM hydrogels, spread on glass coverslips and cultured in DMEM with 10% FBS and 1% PSG in presence of the different treatments for 10 d, were fixed with 4% PFA at 4 °C overnight, permeabilized with 0.5% Triton™ X-100 (Thermo Fisher Scientific), blocked with blocking buffer (BioGeneX), and incubated with primary antibodies against alpha smooth muscle actin (anti-αSMA [ab5694] 1:200; Abcam), followed by incubation with an Alexa Fluor® 488-conjugated secondary antibody; nuclei were counterstained with DAPI (both Abcam). Similarly, constructs were stained with Phalloidin-iFluor 488 (Abcam), nuclei were counterstained with DAPI, according to the manufacturer's instructions. Coverslips were transferred to 35-mm glass bottom dishes (MatTek, Ashland, MA, USA), and fluorescent images were acquired with an Eclipse N*i* or T*i* microscope (Nikon).

2.15. HTM hydrogel histology and immunohistochemistry analyses

HTM/GTM hydrogels, cultured in DMEM with 10% FBS and 1% PSG in presence of the different treatments for 7/10 d were fixed in 4% PFA at 4 °C overnight, followed by incubation in 30% sucrose for 24 h at 4 °C, washed with DPBS, embedded in Tissue-Plus™ O.C.T. Compound (Fisher Scientific), and flash frozen in liquid nitrogen. Twenty micrometer cryosections were cut using a cryostat (Leica Biosystems Inc., Buffalo Grove, IL, USA) and collected on Superfrost™ Plus microscope slides (Fisher Scientific). Sections were stained with standard Hematoxylin & Eosin (H&E) or Picrosirius Red/Hematoxylin (PSR) using the

Picrosirius Red Stain Kit (PolySciences, Warrington, PA, USA) following the manufacturer's protocols. Slides were mounted with Permount™ (Fisher Scientific) and brightfield images were captured with an Eclipse E400 microscope (Nikon). For immunohistochemistry analyses, sections were permeabilized with 0.5% Triton™ X-100, blocked with blocking buffer, and incubated with primary antibodies against fibronectin (anti-fibronectin [ab45688] 1:500; Abcam) or collagen type IV (anti-collagen IV [ab6586] 1:500; Abcam) followed by incubation with an Alexa Fluor® 488-conjugated secondary antibody; nuclei were counterstained with DAPI (both Abcam). Slides were mounted with ProLong™ Gold Antifade (Thermo Fisher Scientific), and fluorescent images were acquired with an Eclipse N*i* microscope (Nikon). Three fields of view per sample were analyzed to quantify normalized fibronectin signal intensity, followed by calculation of fold-change vs. control.

2.16. HTM hydrogel rheology analysis

Fifty microliters of HTM cell-laden or acellular hydrogel precursor solutions were pipetted into custom 8x1-mm PDMS molds (Suppl. Fig. S3). Similarly, 150 μl of HTM/GTM cell-laden hydrogel precursor solutions were pipetted into 24-well culture plates. All samples were UV crosslinked and equilibrated as described above. Acellular hydrogels were measured on 0 d. HTM/GTM hydrogels, cultured in DMEM with 10% FBS and 1% PSG in presence of the different treatments, were measured on 0 d and 7/10 d; samples were cut to size using an 8-mm diameter tissue punch. A Kinexus rheometer (Malvern Panalytical, Westborough, MA, USA) fitted with an 8-mm diameter parallel plate was used to measure hydrogel viscoelasticity. To ensure standard conditions across all experiments (N = 3 per group), the geometry was lowered into the hydrogels until a calibration normal force of 0.02 N was achieved. Subsequently, an oscillatory shear-strain sweep test (0.1–60%, 1.0 Hz, 25 °C) was applied to determine storage modulus (G') and loss modulus (G") in the linear region. Compression testing was performed at axial strains from 0% to −50% by changing the gap between the plates followed by applying a sinusoidal shear strain of 2% at a frequency of 1.0 Hz to determine storage modulus (G') with increasing axial strain.

2.17. Statistical analysis

Individual sample sizes are specified in each figure caption. Comparisons between groups were assessed by unpaired *t*-test, one-way or two-way analysis of variance (ANOVA) with Tukey's multiple comparisons *post hoc* tests, as appropriate. All data are shown with mean ± SD, some with individual data points. The significance level was set at p < 0.05 or lower. GraphPad Prism software v8.4 (GraphPad Software, La Jolla, CA, USA) was used for all analyses.

3. Results

3.1. HTM cell characterization

A reliable feature of HTM cells *in vitro* is upregulation of MYOC expression in more than 50% of cells in response to challenge with the corticosteroid DEX (Keller et al., 2018). Three strains (HTM01, HTM12, HTM19) were used and compared to a validated reference strain (HTM129). All of our HTM cell strains exhibited normal morphology (i. e., cobblestone-like pattern with some overlapping processes; Fig. 2A) and growth characteristics (i.e., contact inhibited with doubling time of ~2 d) comparable to the reference standard. Significantly increased MYOC mRNA expression by qRT-PCR was observed with DEX treatment vs. controls across HTM cell strains (Suppl. Fig. S4). Qualitative assessment of secreted MYOC protein by immunoblot showed robust DEX-inducible expression at 7 d (Fig. 2B and C). It is plausible that overall DEX-induced MYOC upregulation determined by these techniques could be driven by a small number of high-expressing HTM cells. Therefore, we next measured intracellular MYOC expression by
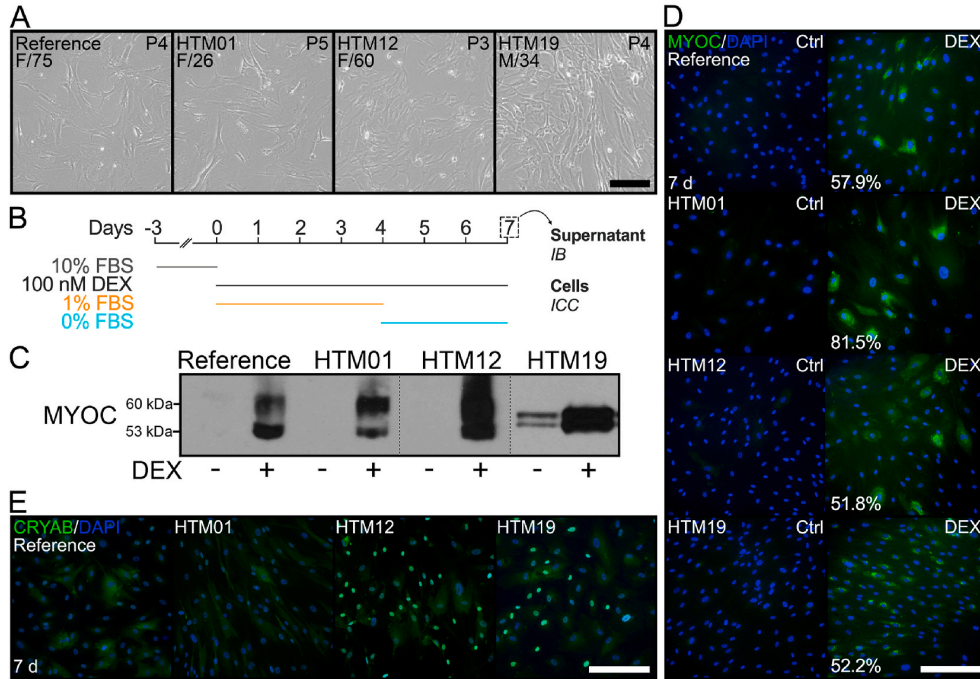
Fig. 2. HTM cell characterization. (A) Representative phase contrast micrographs of reference, HTM01, HTM12, and HTM19 cell strains with sex/age information. Scale bar, 250 μm. (B) Experimental design and timeline. (C) Immunoblot of secreted MYOC at 7 d. (D) Representative fluorescence micrographs of intracellular MYOC at 7 d (MYOC = green; DAPI = blue). Scale bar, 250 μm. (E) Representative fluorescence micrographs of CRYAB (CRYAB = green; DAPI = blue). Scale bar, 250 μm. (For interpretation of the references to colour in this figure legend, the reader is referred to the Web version of this article.)

immunocytochemistry and found significantly increased levels with DEX treatment vs. controls (p < 0.001 for all HTM cell strains; Fig. 2D). Alpha B-Crystallin (CRYAB) is exclusively expressed in the JCT region of the HTM (Siegner et al., 1996). Collagenase was used to digest the dissected strips of HTM tissue; specifically, to disrupt contacts between JCT-HTM cells and their dense ECM, and to encourage cell migration out of the HTM tissue. Our results showed that all of our HTM cell strains and the reference cells highly expressed CRYAB (Fig. 2E), suggesting that a significant population of cells were derived from the JCT layer.

Together, these data suggest that HTM01, HTM12, and HTM19 exhibit all required key characteristics according to a recent consensus paper (Keller et al., 2018) to faithfully identify them as normal HTM cells, comparable to a confirmed reference standard.

3.2. ELP characterization

Upon receipt of the unique ELP construct, the correct nucleotide sequence was confirmed (Suppl. Fig. S1A). Molecular weight analysis of the purified ELP showed the expected 31.2 kDa band with negligible impurities consistent with the original report (Suppl. Fig. S1B) (Zhang et al., 2015). Importantly, the ELP possesses the elastic properties of native elastin via a ([VPGVG]$_4$[IPGVG])$_{14}$ core sequence flanked by KCTS residues in which the cysteines provide the thiol groups to render it UV-crosslinkable. This ELP, together with the commercial methacrylate-conjugated collagen type I and thiol-conjugated hyaluronic acid constitute the photocrosslinkable hydrogel used herein (Suppl. Fig. S2; Fig. 1).

3.3. HTM hydrogel optimization

The number of HTM cells in native tissue decreases with aging. A steady decline from (0.59–1.74) × 10^6 cells/ml in 20-year-old individuals to (0.31–0.92) × 10^6 cells/ml in 80-year-old individuals has

been shown (Abu-Hassan et al., 2014; Tektas and Lütjen-Drecoll, 2009). Therefore, we used a normalized density of 1.0×10^6 cells/ml in HTM cell-laden hydrogels independent of donor age. To ascertain that HTM cells could withstand the UV light-activated free-radical crosslinking process, HTM cell viability in hydrogels crosslinked for increasing times was determined by live/dead staining. Hydrogel-encapsulated HTM01 cells displayed high viability immediately after photocrosslinking (0 d); we observed negligible cell death after 1 s and 5 s of UV crosslinking, and more than 80% cells remained viable after 10 s and 20 s of irradiation. In contrast, significant cell death was noted after 30 s of UV crosslinking (Suppl. Fig. S5A and B).

HTM cells interact with and contract their ECM environment (Ramos et al., 2009). We observed an inverse relationship between UV crosslinking time and HTM hydrogel contraction; i.e., constructs showed highest degree of contraction with shortest crosslinking time (Suppl. Fig. S5). HTM01 hydrogels crosslinked for 1–10 s significantly contracted over culture time, reaching ~40–50% of their original size by 7 d. No differences between constructs irradiated for 1 s and 5 s were found, but hydrogels formed using 10–30 s of UV exposure were significantly less contracted (Suppl. Fig. S5C and D). Constructs in the 20 s group approximated 80% of their baseline size by 7 d, whereas HTM01 hydrogels crosslinked for 30 s exhibited virtually no contraction (Suppl. Fig. S5C and D). This was linked to major cytotoxicity at this time point that interfered with cell spreading/function; while HTM01 cell viability after initial hydrogel formation was ~79%, by 7 d less than 10% of viable cells remained (Suppl. Fig. S5E).

A key advantage of using hydrogels to assess cellular behaviors vs. traditional 2D or scaffold-based 3D culture systems is their viscoelastic behavior (Caliari and Burdick, 2016). Hydrogels showed tissue-like viscoelastic properties by rheology independent of UV crosslinking time, with significantly higher shear storage moduli (G') vs. loss moduli (G") indicating predominantly elastic rather than viscous characteristics. We observed a relationship between UV crosslinking time and

hydrogel stiffness; i.e., constructs showed highest G' values with longest crosslinking time, while G'' remained relatively stable (Suppl. Fig. S6).

Taken together, consistent hydrogel formation was observed with 5 s UV crosslinking. These cytocompatible conditions created a supportive 3D environment enabling normal HTM cell function aided by the adequately soft biomaterial properties. Therefore, 5 s UV crosslinking time was chosen for all following experiments.

3.4. HTM cell viability, contractility, and proliferation in hydrogels

Using the optimized conditions, we next characterized HTM hydrogels made using three different cell strains (HTM01, HTM12, and HTM19) with regard to cell viability, contractility, and proliferation within the 3D biopolymer network. Across all HTM strains, similarly high cell viability exceeding 90% was observed immediately after initial hydrogel formation (0 d) (Fig. 3A and B). Longitudinal contractility quantification showed significant hydrogel contraction with all three HTM cell strains over time, reaching ~20–40% of their original size by 7 d indicating normal donor-to-donor variability (Fig. 3C and D). This was accompanied by near linear cell proliferation in hydrogels over 7 d, at which point negligible cell death and prominent cell spreading were observed with all three HTM cell strains (Fig. 3E and F).
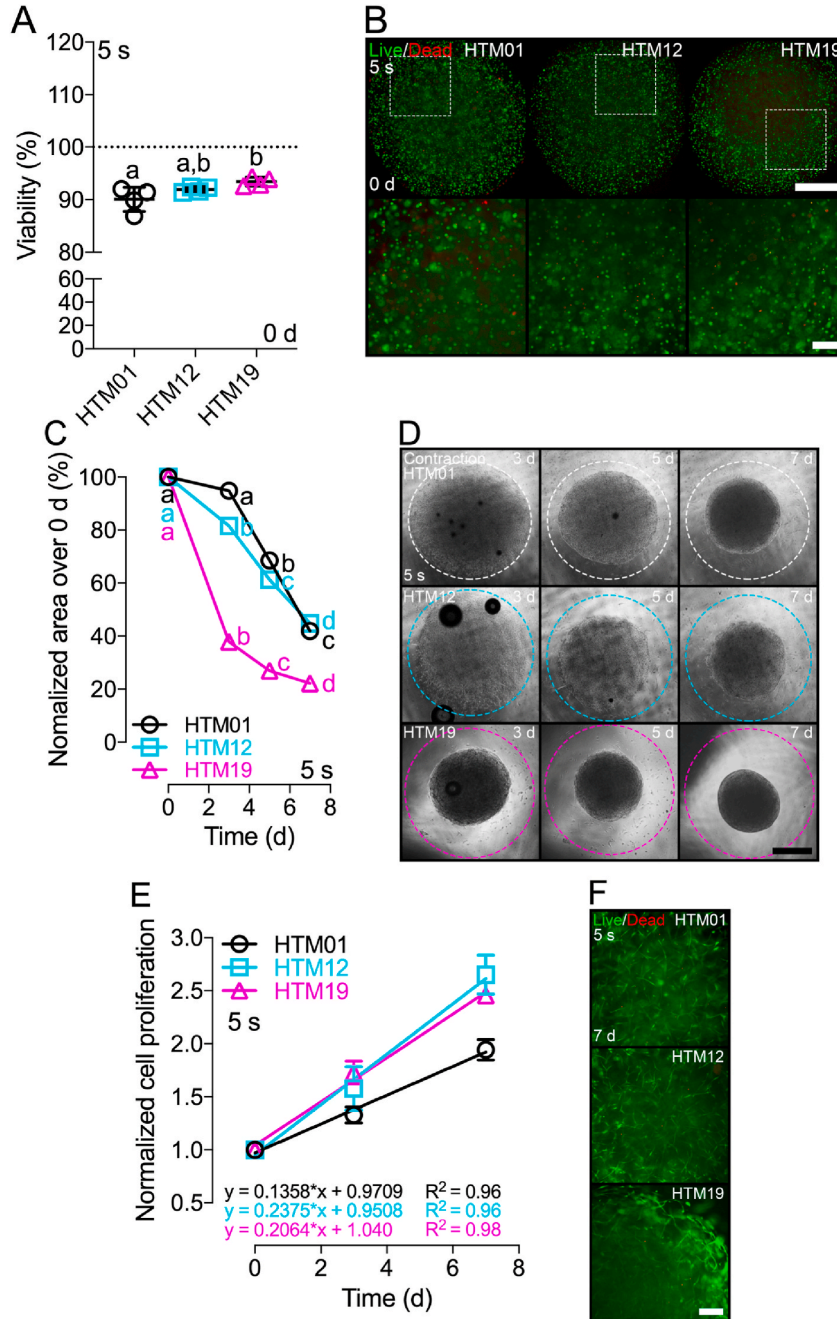

Fig. 3. HTM cell viability, contractility, and proliferation in hydrogels. (A) Cell viability quantification of hydrogel-encapsulated HTM01, HTM12, and HTM19 cells UV-crosslinked for 5 s at 0 d (N = 4 per donor; dotted line shows 100% viability for reference; shared significance indicator letters represent non-significant difference ($p > 0.05$), distinct letters represent significant difference ($p < 0.05$)). (B) Representative fluorescence micrographs of HTM01, HTM12, and HTM19 hydrogels at 0 d (live cells = green; dead cells = red). Scale bars, 1 mm (top) and 250 μm (bottom) (C) Longitudinal quantification (i.e., construct size relative to 0 d). of HTM01, HTM12, and HTM19 cell contractility in hydrogels (N = 3 per donor; shared significance indicator letters represent non-significant difference ($p > 0.05$), distinct letters represent significant difference ($p < 0.05$)). (D) Representative brightfield images of HTM01, HTM12, and HTM19 hydrogels at 3, 5, and 7 d; dashed lines outline original size of constructs at 0 d. Scale bar, 1 mm. (E) Longitudinal cell proliferation quantification of HTM01, HTM12, and HTM19 hydrogels (N = 3 per group and donor; shared significance indicator letters represent non-significant difference ($p > 0.05$), distinct letters represent significant difference ($p < 0.05$)). (F) Representative fluorescence micrographs of HTM01, HTM12 and HTM19 hydrogels at 7 d (live cells = green; dead cells = red). Scale bar, 250 μm. (For interpretation of the references to colour in this figure legend, the reader is referred to the Web version of this article.)

3.5. HTM hydrogel microstructural and mechanical properties

HTM cells within the JCT region reside in a loose connective tissue comprised of reticular and elastic fibers, and ground substance made of proteoglycans and glycosaminoglycans. Pore sizes across the JCT have been estimated at ~2–15 μm (Abu-Hassan et al., 2014; Acott and Kelley, 2008; Hann and Fautsch, 2011; Keller and Acott, 2013; Tamm, 2009). To assess the hydrogel microarchitecture, SEM images were acquired at 0 d (i.e., immediately after 5 s UV crosslinking). Acellular hydrogels exhibited a honeycomb-like architecture with 43.3 ± 27.3 μm pore size (Fig. 4A), comparable to a recently reported hydrogel made of ELP and HA (Shirzaei Sani et al., 2018). For correlative analyses, we next assessed hydrogel mechanical properties by rheology of both acellular and HTM cell-encapsulated hydrogels (HTM12 and HTM19). In general, hydrogel stiffness is dependent on biopolymer concentrations/arrangement and crosslinking density (Suppl. Fig. S6), with encapsulated contractile cells further contributing to construct elasticity. At the chosen crosslinking time of 5 s, we observed overall relatively low modulus values in the low pascal-range, consistent with the low-to-medium biopolymer concentrations used. HTM cell-encapsulated hydrogels were significantly stiffer compared to acellular samples independent of the HTM cell strain used, while G" was comparable (Fig. 4B). Regardless of whether or not cells were present within the 3D biopolymer network, hydrogels displayed tissue-like compression stiffening (van Oosten et al., 2019); i.e., increase in shear modulus with increasing compressive strain (Fig. 4C).

These data show that our HTM hydrogel provides an adequately porous and soft 3D microenvironment that mimics the mechanical properties of native heterogeneous soft connective tissues.

3.6. HTM hydrogels as glaucoma disease model: pharmacological induction/rescue

3.6.1. Hydrogel contractility

The contractility status of HTM cells and overall tissue influences AH outflow resistance and IOP (Dismuke et al., 2014). Increased HTM contraction is observed in patients with POAG, which typically leads to tissue stiffening, decreased AH outflow facility, and elevated IOP (Tektas and Lütjen-Drecoll, 2009). Steroid therapy is widely used to treat a variety of inflammatory diseases and conditions. However, long term use of ocular corticosteroids such as DEX often results in elevated IOP and POAG (Overby and Clark, 2015). To ascertain whether photocrosslinked HTM hydrogels could serve as a glaucoma disease model, we treated constructs with DEX (Keller et al., 2018) to induce POAG-like conditions and evaluated its effects on hydrogel contractility. In the United States, the ROCK inhibitor netarsudil is a clinically available drug that directly targets the stiffened HTM to increase AH outflow via cell/tissue relaxation (Rao et al., 2001, 2017; Serle et al., 2018; Tanna and Johnson, 2018; Wang and Chang, 2014). Therefore, we assessed the effects of ROCK inhibitor Y27632 treatment on HTM hydrogel contractility using three different cell strains (HTM01, HTM12, and HTM19) following DEX induction.

We observed significant contraction over time in all groups independent of the HTM cell strain used (Fig. 5A–C; Suppl. Fig. S7A-C). DEX-treated HTM hydrogels exhibited significantly greater contraction vs. controls by 5 d, reaching ~30–44% of their original size, that was influenced by donor-to-donor variability. Comparable values were found in the sequential treatment samples (DEX (5 d) + Y27632 (5 d)), which at this point had only been exposed to DEX rendering the two groups virtually identical (all below controls). In contrast, Y27632 significantly relaxed the HTM hydrogels (i.e., decreased contraction; ~65–77% of their original size) vs. controls. Small differences were noted between DEX + Y27632 co-treated samples and controls by 5 d, displaying significantly less contraction compared to DEX- and DEX (5 d) + Y27632 (5 d)-treated HTM hydrogels, yet significantly more contraction vs. Y27632-treated constructs; this suggests that Y27632 can prevent DEX-induced pathologic contraction of HTM hydrogels when presented together (Fig. 5D-I; Suppl. Fig. S7A-C).

Overall similar trends were observed at 10 d (Fig. 5J–O; Suppl. Fig. S7A-C). DEX treatment induced notably more contraction (~16–25% of their original size; statistically significant for HTM12), whereas Y27632 treatment resulted in significantly less contraction
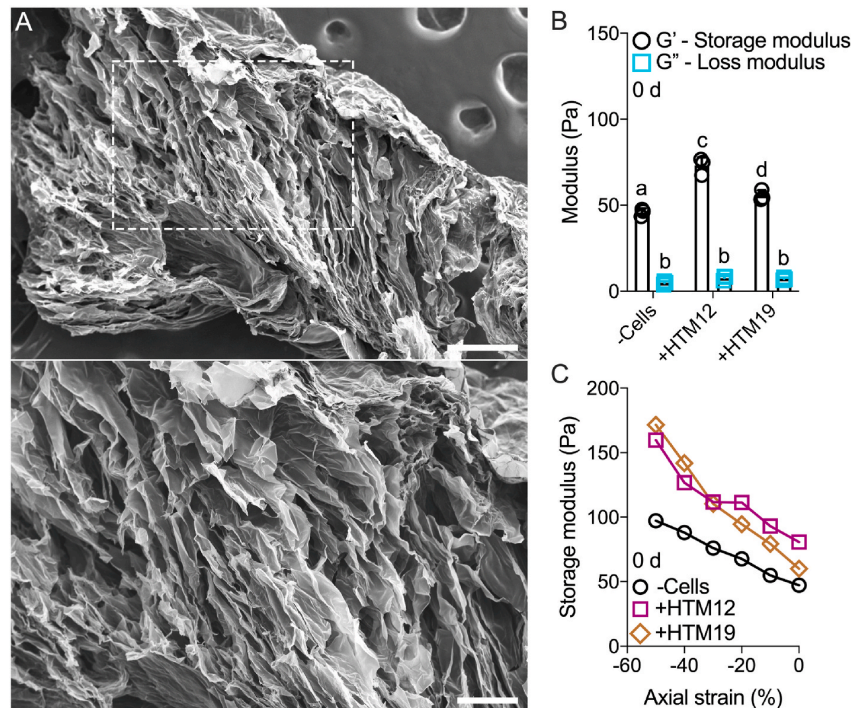

Fig. 4. HTM hydrogel microstructural and mechanical analyses. (A) Scanning electron micrographs of acellular hydrogels UV-crosslinked for 5 s at 0 d (dashed box shows region of interest in higher magnification image). Scale bars, 250 μm (top) and 100 μm (bottom). (B) Storage and loss moduli of acellular and HTM12 or HTM19 cell-encapsulated hydrogels UV-crosslinked for 5 s at 0 d (N = 4 per group/donor; shared significance indicator letters represent non-significant difference (p > 0.05), distinct letters represent significant difference (p < 0.05)). (C) Storage modulus measured at 2% shear strain as a function of axial strain for acellular and HTM12 or HTM19 cell-encapsulated hydrogels at 0 d (N = 3 per group/donor).
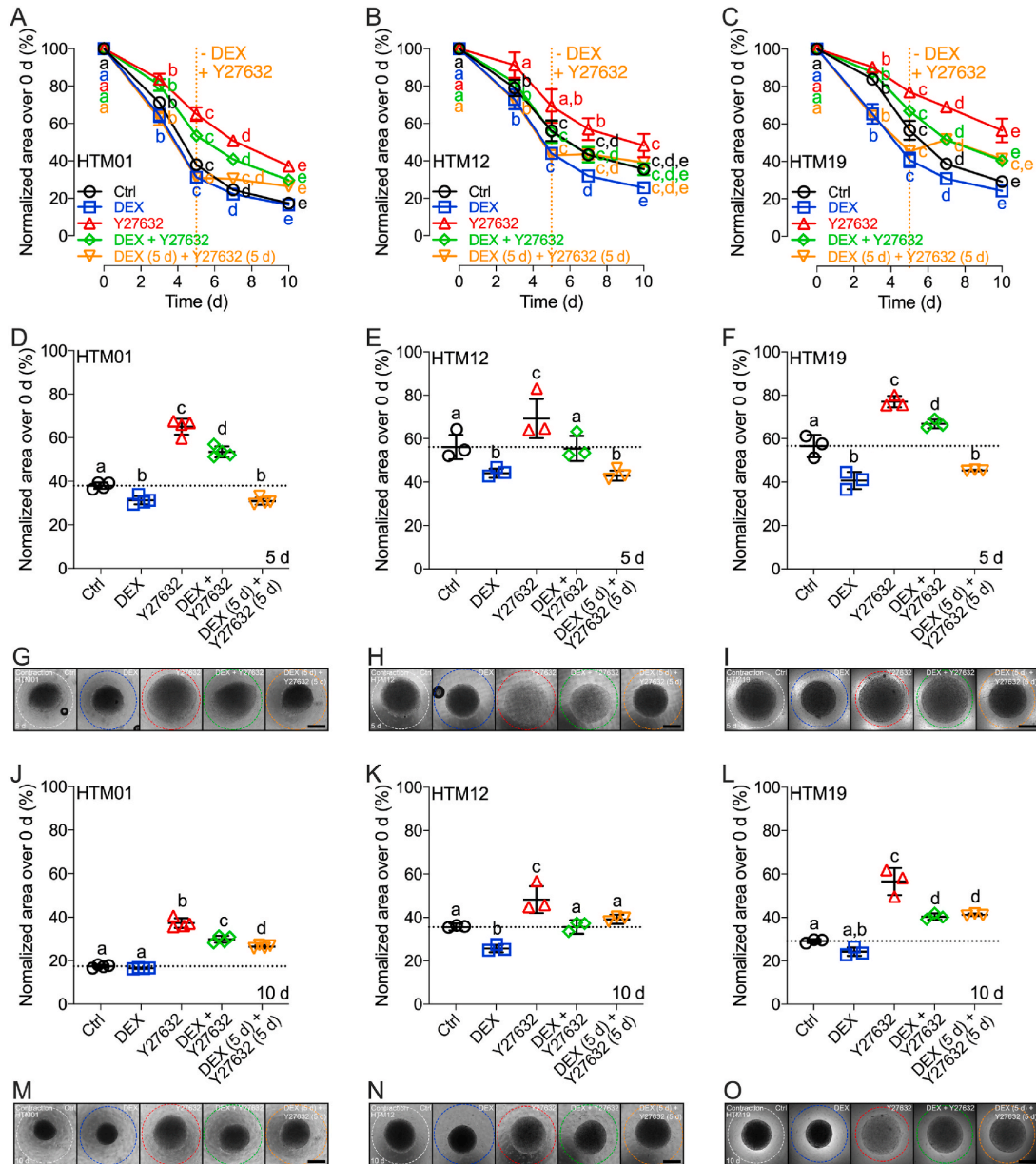
Fig. 5. HTM cell contractility in hydrogels with corticosteroid induction and ROCK inhibitor rescue. Longitudinal quantification (i.e., construct size relative to 0 d) of (A) HTM01, (B) HTM12, and (C) HTM19 cell contractility in hydrogels UV-crosslinked for 5 s subjected to control, 100 nM DEX, 10 μM Y27632, DEX + Y27632, or DEX (5 d) + Y27632 (5 d) (N = 3–4 per group and donor; shared significance indicator letters represent non-significant difference (p > 0.05), distinct letters represent significant difference (p < 0.05)). Detailed comparisons between groups at 5 d in (D) HTM01, (E) HTM12, and (F) HTM19 hydrogels (N = 3–4 per group and donor; dotted lines show respective control values for reference; shared significance indicator letters represent non-significant difference (p > 0.05), distinct letters represent significant difference (p < 0.05)). Representative brightfield images of (G) HTM01, (H) HTM12, and (I) HTM19 hydrogels subjected to the different treatments at 10 d (dashed lines outline original size of constructs at 0 d. Scale bars, 1 mm). Detailed comparisons between groups at 10 d in (J) HTM01, (K) HTM12, and (L) HTM19 hydrogels (N = 3–4 per group and donor; dotted lines show respective control values for reference; shared significance indicator letters represent non-significant difference (p > 0.05), distinct letters represent significant difference (p < 0.05)). Representative brightfield images of (M) HTM01, (N) HTM12, and (O) HTM19 hydrogels subjected to the different treatments at 10 d (dashed lines outline original size of constructs at 0 d. Scale bars, 1 mm).

(~37–56% of their original size) vs. all other groups. Again, small differences were observed between DEX + Y27632 co-treatment and controls. Importantly, in a clinical scenario, the HTM tissue would likely already show signs of dysfunction before any POAG treatment would be administered. We simulated this with the sequential treatment group: DEX induction for 5 d followed by Y27632 treatment for 5 d with DEX withheld. Our results showed that Y27632 rescued HTM hydrogel

contraction induced by DEX and prevented further contraction; i.e., construct size with DEX (5 d) + Y27632 (5 d) sequential treatment was similar to the control and DEX + Y27632 groups, but significantly increased compared to DEX-treated samples (Fig. 5J–O; Suppl. Fig. S7A-C).

Next, to see if hydrogel contractility was influenced by the cell number, we assessed HTM cell proliferation (HTM12 and HTM19) in

constructs subjected to the different treatments. For HTM12 hydrogels, cells in the DEX-treated group showed significantly less proliferation compared to the Y27632 treated group at 10 d, while no significant differences were observed across all other groups (Suppl. Fig. S7D). No differences between groups were found for HTM19 hydrogels (Suppl. Fig. S7E).

Together, this suggests that DEX robustly induces HTM hydrogel contractility mimicking glaucomatous conditions across multiple donor cell strains, and that ROCK inhibition prevents or rescues DEX-induced pathologic contraction.

3.6.2. Hydrogel actin rearrangement

The actin cytoskeleton, the primary force-generating machinery in cells, plays fundamental roles in various cellular process such as migration, morphogenesis, and cytokinesis (Svitkina, 2018). Filamentous f-actin fiber arrangement directly affects cell and tissue contraction.
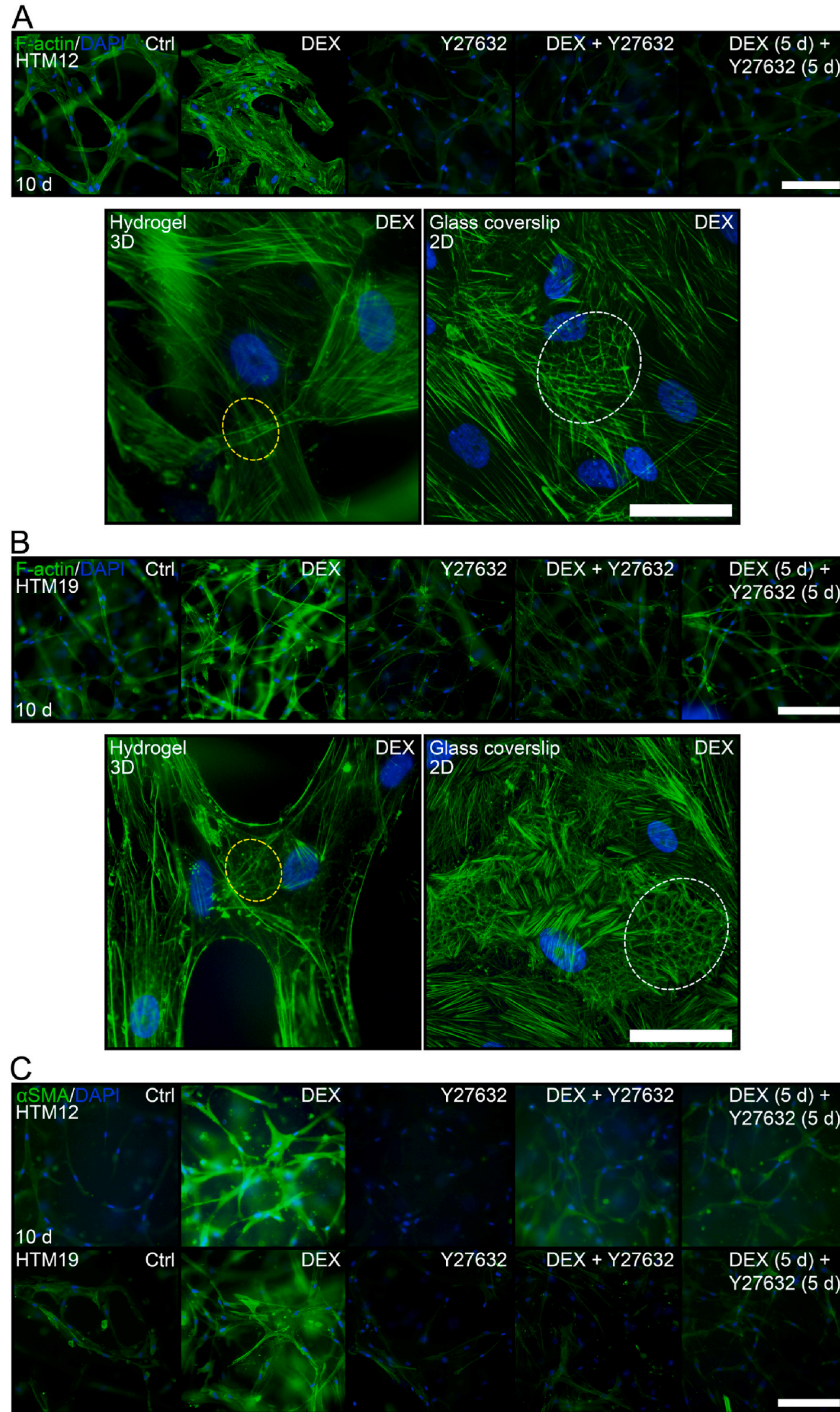

Fig. 6. HTM cell f-actin and αSMA expression in hydrogels with corticosteroid induction and ROCK inhibitor rescue. Representative fluorescence micrographs of f-actin in (A) HTM12 and (B) HTM19 hydrogels UV-crosslinked for 5 s subjected to control, 100 nM DEX, 10 μM Y27632, DEX + Y27632, or DEX (5 d) + Y27632 (5 d) at 10 d (f-actin = green; DAPI = blue). Scale bars, 250 μm. High magnification images of DEX-treated HTM hydrogels showing differentially organized f-actin structures (yellow dashed outlines) or HTM cells on glass coverslips to illustrate formation of crosslinked actin networks (white dashed outlines). Scale bars, 50 μm. (C) Representative fluorescence micrographs of αSMA in HTM12 and HTM19 hydrogels subjected to the different treatments at 10 d (αSMA = green; DAPI = blue). Scale bars, 250 μm. (For interpretation of the references to colour in this figure legend, the reader is referred to the Web version of this article.)

Therefore, we next investigated f-actin and αSMA abundance and organization in HTM hydrogels (HTM12 and HTM19) subjected to the different treatments (Fig. 6). Independent of the HTM cell strain used, DEX-treated constructs showed qualitatively increased formation and different organization of f-actin fibers in the 3D hydrogel environment vs. controls. Expected crosslinked actin networks (white dashed outlines) were abundant and readily identified in DEX-treated HTM12 and HTM19 cells cultured on 2D glass coverslips, corresponding with differentially organized f-actin in the DEX-treated 3D hydrogels (yellow dashed outlines) (Fig. 6A and B). Y27632 treatment notably reduced f-actin fibers in HTM12 and HTM19 hydrogels compared to both control and DEX-treated groups. No differences were observed for DEX + Y27632 co- or sequential treatment in comparison to Y27632; again markedly decreased f-actin fibers were noted vs. control and DEX-treated groups (Fig. 6A and B).

Overall relatively similar trends were observed for αSMA. DEX-treated samples showed substantially increased αSMA expression vs. all other groups, whereas Y27632 nearly abolished the αSMA signal (high exposure chosen to illustrate this point in HTM12 hydrogels). Again, no differences were observed between DEX + Y27632 co- or sequential treatment, with comparable αSMA expression in HTM12 or HTM19 hydrogels to controls, but slightly higher levels vs. Y27632-treated hydrogels (Fig. 6C).

Together, these data show that DEX increases f-actin fibers and αSMA in HTM hydrogels independent of the donor cell strain used, which is potently rescued by Y27632. This is consistent with the reported reduction of actomyosin contractile tone in HTM tissue following ROCK inhibition (Rao et al., 2001, 2017; Tanna and Johnson, 2018; Wang and Chang, 2014). These changes in f-actin and αSMA could have a direct impact on HTM cell contractility and interactions with their surrounding ECM, as well as HTM tissue stiffness and ultimately AH outflow resistance.

3.6.3. Hydrogel morphology and ECM deposition

Continuous remodeling of baseline hydrogel ECM components (i.e., fibrillar collagen type I and ELP, plus HA) and HTM cell-secreted ECM over culture time, and in response to the different treatments, is expected and desired. We next investigated overall morphology of HTM hydrogels (HTM12 and HTM19) subjected to the different treatments using hematoxylin & eosin- and picrosirius red-stained sections (Suppl. Fig. S8A and B). Consistent with the contractility analyses, DEX-treated HTM12 hydrogels appeared morphologically more condensed. By contrast, Y27632 qualitatively increased the network spacing compared to controls. DEX + Y27632 co- or sequential treatment groups were comparable to controls but qualitatively less dense vs. DEX-treated constructs. Abundant hematoxylin-stained HTM cells were visible across groups. The overall morphology of HTM19 hydrogels was relatively comparable across groups; hydrogels appeared slightly denser compared to HTM12 samples (Suppl. Fig. S8A and B), highlighting inherent donor-to-donor variability.

There is increased accumulation of ECM proteins in the HTM tissue of glaucomatous eyes (Stamer and Clark, 2017). Therefore, we next evaluated HTM cell-mediated fibronectin deposition within hydrogels (HTM12 and HTM19) in response to the different treatments (Fig. 7). In HTM12 hydrogels, DEX-treated constructs exhibited significantly more fibronectin deposition vs. controls, whereas Y27632 markedly reduced the fibronectin signal intensity. DEX + Y27632 co-treatment resulted in significantly less fibronectin deposition compared to the control and DEX groups. Importantly, Y27632 rescued aberrant fibronectin deposition induced by DEX; i.e., significantly less signal intensity with DEX (5 d) + Y27632 (5 d) sequential treatment was noted compared to DEX-treated samples (Fig. 7A and B). Relatively similar trends were observed for HTM19 hydrogels; DEX-treated constructs again showed significantly higher fibronectin deposition vs. controls. Fibronectin levels with Y27632 treatment were comparable to controls. DEX +
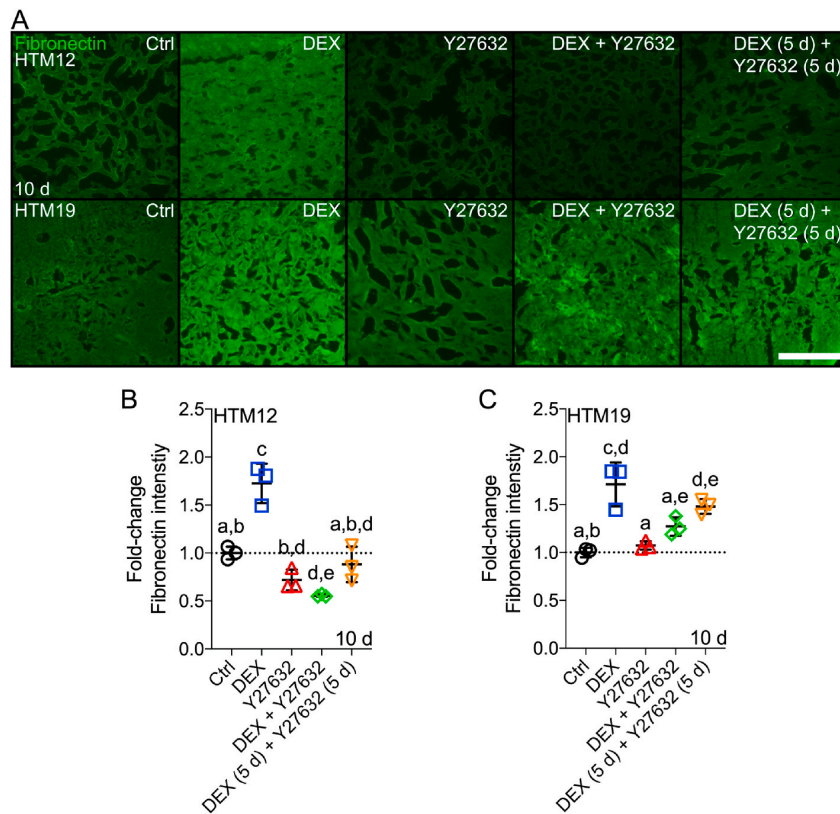

Fig. 7. HTM cell fibronectin deposition in hydrogels with corticosteroid induction and ROCK inhibitor rescue. (A) Representative fluorescence micrographs of fibronectin deposition (= green) in HTM12 and HTM19 hydrogels UV-crosslinked for 5 s subjected to control, 100 nM DEX, 10 μM Y27632, DEX + Y27632, or DEX (5 d) + Y27632 (5 d) at 10 d. Scale bar, 250 μm. Quantification of fibronectin deposition in (B) HTM12 and (C) HTM19 hydrogels subjected to the different treatments at 10 d (N = 3 per group; dotted lines show respective control values for reference; shared significance indicator letters represent non-significant difference (p > 0.05), distinct letters represent significant difference (p < 0.05)). (For interpretation of the references to colour in this figure legend, the reader is referred to the Web version of this article.)

Y27632 co- or sequential treatment groups exhibited higher fibronectin deposition than controls but overall less vs. DEX-treated constructs (Fig. 7A,C). These observations suggest a differential response of fibronectin secretion to ROCK inhibition in HTM19 vs. HTM12 hydrogels, consistent with donor-to-donor variability seen with other readouts. An overall comparable collagen IV deposition pattern was found in HTM12 and HTM19 hydrogels (Suppl. Fig. S8C).

Together, these data show that DEX induces HTM hydrogel condensation and remodeling, and aberrant ECM deposition across multiple donor cell strains consistent with glaucomatous tissue dysfunction, which is largely rescued with ROCK inhibition.

3.6.4. Hydrogel stiffening

Dysregulation of HTM cells and pathologic ECM remodeling jointly contribute to HTM stiffening in POAG, which negatively affects IOP in a positive feedback loop (Last et al., 2011; Stamer and Acott, 2012; Wang et al., 2017a). To assess the functional consequences of increased hydrogel contraction/condensation, driven by cytoskeletal rearrangements and ECM remodeling/deposition, on tissue-level construct stiffness, we next performed rheology analysis of HTM hydrogels (HTM12 and HTM19) subjected to the different treatments to determine storage moduli (Fig. 8). DEX treatment significantly stiffened HTM hydrogels vs. control ($\sim$1.7-fold for HTM12 hydrogels; $\sim$1.5-fold for HTM19 hydrogels; Fig. 8A and B) consistent with recent reports of glaucomatous HTM tissue behavior (Wang et al., 2017a, 2017b), while Y27632 had precisely opposite effects and significantly softened HTM hydrogels vs. controls ($\sim$0.6-fold for HTM12 hydrogels; $\sim$0.4-fold for HTM19 hydrogels; Fig. 8A and B). No differences were observed between DEX + Y27632 co-treatment and controls. Importantly, Y27632 rescued pathologic HTM hydrogel stiffening induced by DEX, independent of the donor cell strain used, and prevented further stiffening; i.e., storage modulus with DEX (5 d) + Y27632 (5 d) sequential treatment was similar to the control and DEX + Y27632 groups, but significantly lower compared to DEX-treated samples (Fig. 8A and B). These findings were in agreement with HTM hydrogel contraction, f-actin and αSMA expression, and fibronectin deposition (Figs. 5–7).
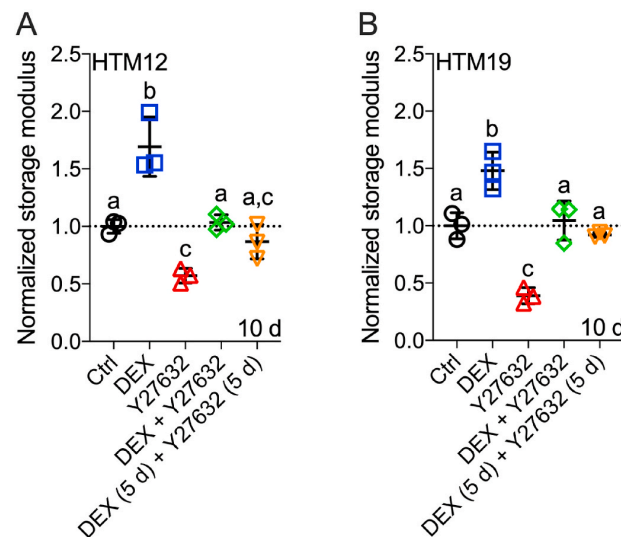

Fig. 8. HTM hydrogel stiffness with corticosteroid induction and ROCK inhibitor rescue. Normalized storage modulus (to controls) of (A) HTM12 and (B) HTM19 hydrogels UV-crosslinked for 5 s subjected to control, 100 nM DEX, 10 μM Y27632, DEX + Y27632, or DEX (5 d) + Y27632 (5 d) at 10 d (N = 3 per group; dotted lines show respective control values for reference; shared significance indicator letters represent non-significant difference (p > 0.05), distinct letters represent significant difference (p < 0.05)).

This suggests that DEX induces tissue-level HTM hydrogel stiffening independent of the donor cell strain used consistent with glaucomatous tissue behavior, and that ROCK inhibition effectively prevents or rescues DEX-induced pathologic stiffening.

3.7. GTM hydrogels as glaucoma disease model: validation

3.7.1. GTM cell characterization and hydrogel encapsulation

Glaucomatous HTM (GTM) cells, isolated from donor eyes with confirmed POAG history, enable relevant studies of HTM cell pathophysiology *in vitro,* possibly without further pharmacological stimulation. GTM1445 cells showed normal morphology but slower growth characteristics (Fig. 9A). Qualitative assessment of intracellular MYOC protein by immunoblot showed robust DEX-inducible expression (Fig. 9B). This was confirmed by quantitative immunocytochemistry analysis; we observed significantly induced MYOC expression with DEX treatment vs. control. Of note, baseline MYOC expression in absence of DEX was markedly elevated ($\sim$40%; Fig. 9C) compared to normal HTM cells (<10%; Fig. 2D), possibly indicative of the cells' disease status. Upon hydrogel encapsulation, GTM1445 cells displayed high viability (94.2%) immediately after 5 s UV crosslinking (0 d) (Fig. 9D), comparable to normal HTM hydrogels (Fig. 3A and B). Markedly slower GTM1445 cell proliferation ($\sim$4.4-fold) vs. normal HTM cells (Fig. 3E and F) was observed over 7 d, at which point there was negligible cell death, yet limited cell spreading throughout the 3D hydrogel network (Fig. 9E and F).

These data show that GTM1445 cells exhibit all required key characteristics (Keller et al., 2018) to identify them as glaucomatous HTM cells, and that our hydrogel system provides a cytocompatible and supportive 3D environment facilitating adequate cell growth and spreading.

3.7.2. GTM hydrogel contractility, proliferation, ECM deposition, and stiffening

To validate our hydrogel system as a glaucoma disease model, we encapsulated GTM1445 cells for comparisons with normal HTM12 hydrogels (best possible "age match") under non-induced conditions. Furthermore, constructs were treated with DEX to explore the GTM cells' response to further glaucomatous induction, and Y27632 to simulate clinical ROCK inhibition. GTM1445 hydrogels in absence of pharmacological induction showed significantly greater contraction vs. normal HTM12 hydrogels by 10 d, reaching $\sim$30% of their original size (Fig. 10A and B). With DEX-induction, both GTM1445 and HTM12 hydrogels exhibited significant further contraction at comparable rates relative to their respective controls. In contrast, Y27632 significantly relaxed GTM1445 and HTM12 hydrogels (i.e., decreased contraction; $\sim$47% and $\sim$45% of their original size, respectively) vs. control and DEX-treated groups (Fig. 10A and B). GTM1445 hydrogels were significantly less contracted vs. normal HTM12 hydrogels, suggesting greater sensitivity of GTM cells to ROCK inhibition. Notably, pathologic GTM1445 cell contractility in hydrogels was observed despite significantly lower cell numbers than in HTM12 hydrogels across all groups (Fig. 10C). Owing to the GTM cells' apparent "pathologic memory" not requiring additional DEX-induction, we focused on untreated controls and Y27632 for subsequent experiments. Due to an unforeseen technical problem, we evaluated cell-mediated fibronectin deposition and hydrogel stiffness at 7 d rather than 10 d. GTM1445 hydrogels exhibited significantly more fibronectin deposition vs. HTM12 hydrogel controls, while Y27632 significantly reduced the signal intensity to normal baseline levels (Fig. 10D and E). Importantly, GTM1445 hydrogels were significantly stiffened vs. HTM12 hydrogels ($\sim$1.2-fold), and Y27632 treatment significantly softened GTM1445 hydrogels reaching levels similar to normal controls (Fig. 10F).

Together, these data suggest that hydrogel-encapsulated GTM cells in absence of additional stimuli mirror the pathologic behavior of induced normal HTM cells, validating our model.
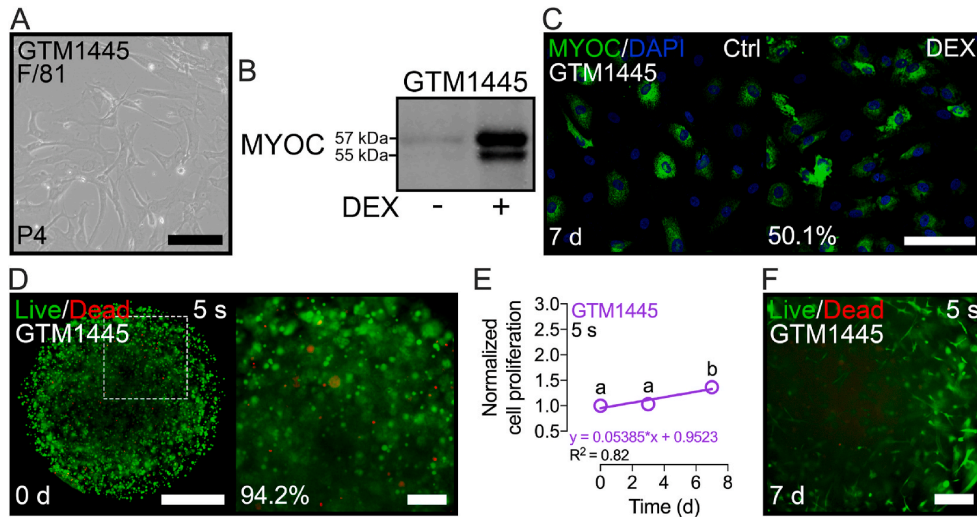
Fig. 9. GTM cell characterization, and viability and proliferation in hydrogels. (A) Representative phase contrast micrograph of GTM1445 cells with sex/age information. Scale bar, 250 μm. (B) Immunoblot of intracellular MYOC at 7 d. (C) Representative fluorescence micrographs of intracellular MYOC at 7 d (MYOC = green; DAPI = blue). Scale bar, 250 μm. (D) Representative fluorescence micrographs of GTM1445 hydrogels UV-crosslinked for 5 s at 0 d (live cells = green; dead cells = red). Scale bars, 1 mm (left) and 250 μm (right). (E) Longitudinal cell proliferation quantification of GTM1445 hydrogels UV-crosslinked for 5 s (N = 4 per group; shared significance indicator letters represent non-significant difference (p > 0.05), distinct letters represent significant difference (p < 0.05)). (F) Representative fluorescence micrographs of GTM1445 hydrogels UV-crosslinked for 5 s at 7 d (live cells = green; dead cells = red). Scale bar, 250 μm. (For interpretation of the references to colour in this figure legend, the reader is referred to the Web version of this article.)

4. Discussion

In vitro studies of HTM cell function are fundamentally limited by traditional cell culture systems. It is widely accepted that cells in 3D environments made of relevant ECM proteins show altered behavior compared to 2D, highlighting the need for more biologically-relevant HTM model systems (Bhadriraju and Chen, 2002; Edmondson et al., 2014). Current bioengineered models (Bouchemi et al., 2017; Dautriche et al., 2015; Osmond et al., 2017, 2020; Saccà et al., 2020; Torrejon et al., 2013, 2016a; Vernazza et al., 2019; Waduthanthri et al., 2019) are useful tools for investigating aspects of HTM cell/tissue behavior under normal and simulated glaucomatous conditions, and complement proven *ex vivo* perfusion-cultured anterior segments and *in vivo* animal models. However, they cannot accurately mimic the complex native HTM cell-ECM interface, which makes them less than ideal to investigate the processes involved in the onset and progression of glaucomatous HTM stiffening typically observed with POAG. In this study, we used a "reductionist approach" and focused on critical ECM proteins present in the native tissue to formulate a novel biomimetic 3D HTM hydrogel to provide a key advancement in bioengineered glaucoma disease modeling.

Our aim was to partially recapitulate the JCT region for both its critical role in regulating AH outflow resistance and IOP, and inextricable link to glaucomatous HTM tissue stiffening. HTM cells within the JCT are surrounded by essential fibrillar ECM components (i.e., collagen type I, elastin) to form a loose connective tissue rich in the glycosaminoglycan HA (Abu-Hassan et al., 2014; Acott and Kelley, 2008; Hann and Fautsch, 2011; Keller and Acott, 2013; Tamm, 2009). We recognize that other important ECM components (e.g., collagen type IV, laminin, fibronectin) contribute to the JCT function; however, their possible - yet not trivial - hydrogel incorporation exceeds the scope of the present study. Proper maintenance of the HTM cell-ECM microenvironment is critical for homeostatic IOP regulation via normal ECM remodeling (Abu-Hassan et al., 2014; Acott and Kelley, 2008; Hann and Fautsch, 2011; Tamm, 2009). Protein-based hydrogels are widely used in tissue engineering applications as they provide a simplified version of the natural 3D tissue environment and allow for accurate *in vitro* modeling

of cellular behaviors (Green and Elisseeff, 2016; Khademhosseini and Langer, 2007; Lee and Mooney, 2001; Seliktar, 2012; Zhang and Khademhosseini, 2017). Photoactive functional groups (e.g., thiols, methacrylates) can be chemically conjugated to protein-based materials. These functionalized precursors can then be crosslinked by exposure to UV light in the presence of a biocompatible photoinitiator, without or with cells, to form stable hydrogel networks with high water content (Zhang and Khademhosseini, 2017). Collagen type I and HA are frequently used for tissue engineering applications and functionalized polymers are commercially available; however, incorporating elastin presents certain challenges. In native tissues, elastic fibers are highly crosslinked and insoluble preventing their direct processing for use in biomaterials (Mithieux and Weiss, 2005). Therefore, various forms of soluble elastin have been engineered, including ELPs (Daamen et al., 2007; Nettles et al., 2010). The key advantage of the unique ELP used herein is that it is flanked by a short peptide sequence (KCTS) in which the two cysteines effectively act as photoactive thiols (Zhang et al., 2015). A UV-crosslinked hydrogel containing ELP and HA was recently reported (Shirzaei Sani et al., 2018); however, no study to date has developed a biopolymer composite system with added collagen type I, the most abundant fibrillar protein in the human body and main structural element of the ECM (Frantz et al., 2010).

We formulated a novel HTM hydrogel by mixing normal human donor-derived TM cells with methacrylate-conjugated collagen type I, KCTS-flanked ELP, and thiol-conjugated HA followed by photoinitiator-mediated short UV crosslinking. The photoactive biopolymers can form chemical crosslinks via methacrylate, thiol-ester, or disulfide linkages. In addition, crosslinking occurs via covalent bond formation between amino acids of collagen fibrils (Tirella et al., 2012), or moieties (C–H, O–H, or N–H groups) in the ELP sequence (Zhang et al., 2015). Informed by previous studies (Mazzocchi et al., 2019), we showed excellent HTM cell viability (i.e., negligible cytotoxicity) in response to 5 s UV crosslinking at the chosen conditions. This protein-based hydrogel created a supportive microenvironment to facilitate prominent HTM cell spreading/proliferation throughout the adequately soft and porous 3D network. Of note, we estimated (acellular) hydrogel pore size at ~40 μm, which is larger than that found in the JCT but consistent with
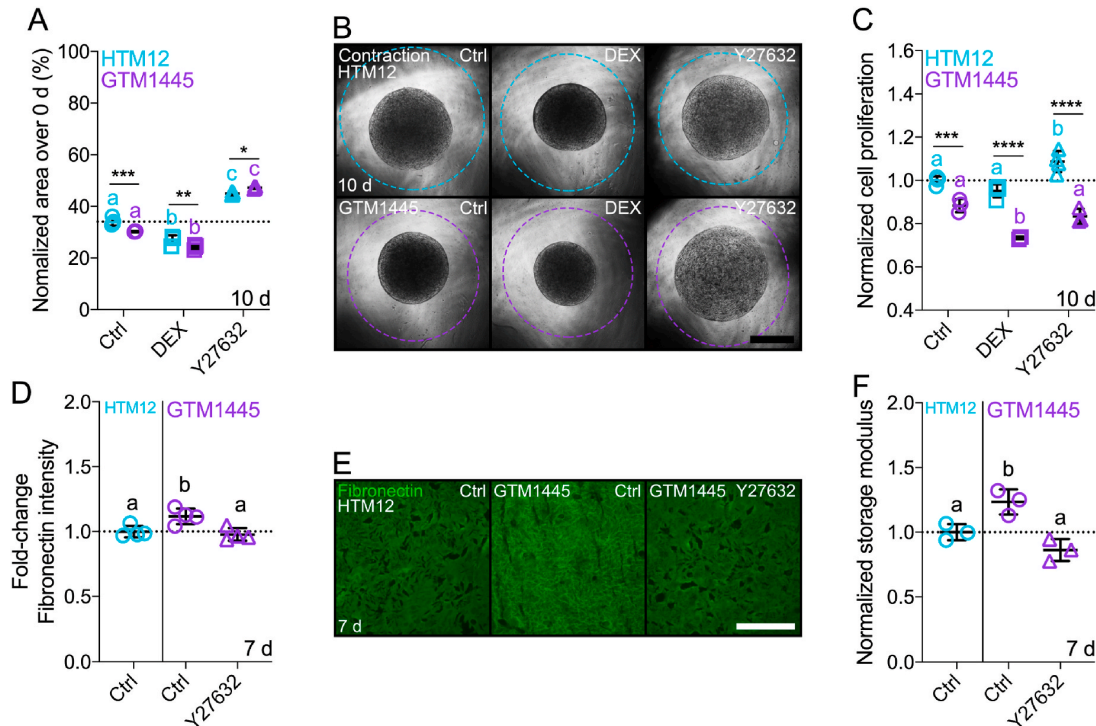
Fig. 10. GTM cell contractility, proliferation, fibronectin deposition, and stiffness of hydrogels with ROCK inhibitor rescue. (A) Contractility of HTM12 and GTM1445 hydrogels UV-crosslinked for 5 s subjected to control, 100 nM DEX and 10 μM Y27632 at 10 d (N = 3 per group and donor; dotted lines show respective control values for reference; *p < 0.05, **p < 0.01, ***p < 0.001 HTM12 vs. GTM1445; shared significance indicator letters represent non-significant difference (p > 0.05), distinct letters represent significant difference (p < 0.05) HTM12 [cyan] or GTM1445 [purple]). (B) Representative brightfield images of HTM12 and GTM1445 hydrogels UV-crosslinked for 5 s subjected to the different treatments at 10 d (white dashed lines outline original size of constructs at 0 d. Scale bar, 1 mm). (C) Cell proliferation quantification of HTM12 and GTM1445 hydrogels UV-crosslinked for 5 s subjected to the different treatments at 10 d (N = 4 per group; ***p < 0.001 HTM12 vs. GTM1445; shared significance indicator letters represent non-significant difference (p > 0.05), distinct letters represent significant difference (p < 0.05) HTM12 [cyan] or GTM1445 [purple]). (D) Quantification of fibronectin deposition in HTM12 hydrogels UV-crosslinked for 5 s subjected to control, and GTM1445 hydrogels subjected to control and 10 μM Y27632 at 7 d (N = 3 per group; dotted lines show respective control values for reference; shared significance indicator letters represent non-significant difference (p > 0.05), distinct letters represent significant difference (p < 0.05)). (E) Representative fluorescence micrographs of fibronectin deposition (= green) in HTM12 and GTM1445 hydrogels UV-crosslinked for 5 s subjected to the different treatments at 7 d. Scale bar, 250 μm. (F) Normalized storage modulus (to controls) of HTM12 and GTM1445 hydrogels UV-crosslinked for 5 s subjected to the different treatments at 7 d (N = 3 per group; dotted lines show respective control values for reference; shared significance indicator letters represent non-significant difference (p > 0.05), distinct letters represent significant difference (p < 0.05)). (For interpretation of the references to colour in this figure legend, the reader is referred to the Web version of this article.)

the central and outer lamellar regions (Abu-Hassan et al., 2014; Acott and Kelley, 2008; Tamm, 2009). Higher concentrations of biopolymer precursors could provide increased crosslinking density, which may increase the hydrogel stiffness and consequently decrease pore size. Dynamic interactions between HTM cells and their surrounding ECM resulted in hydrogel condensation/contraction and remodeling, mimicking critical normal tissue behavior. As such, our HTM cell-encapsulated hydrogel containing (by weight) ~68% collagen type I, ~26% ELP, and ~5% HA is the first of its kind with distinct biomimetic advantages over other HTM model systems (Bouchemi et al., 2017; Dautriche et al., 2015; Osmond et al., 2017, 2020; Saccà et al., 2020; Torrejon et al., 2013, 2016a; Vernazza et al., 2019; Waduthanthri et al., 2019).

Prolonged treatment with ocular corticosteroids such as DEX can lead to steroid-induced elevation of IOP. This in turn can cause steroid-induced glaucoma, which has commonalities with POAG; namely, increased HTM cell/tissue contraction and ECM deposition that can lead to HTM stiffening and increased resistance to AH outflow (Faralli et al., 2019; Johnson et al., 1990; Johnson, 2006; Ramos et al., 2009). Therefore, DEX is frequently used to induce glaucomatous conditions in experimental studies (Rybkin et al., 2017). Rho-associated kinases are effectors of the small GTPase Rho, which play major roles in mediating

the reorganization of the actin cytoskeleton (Leung et al., 1995; Riento and Ridley, 2003) with involvement in diseases such as pulmonary hypertension, nerve injury, and POAG (Amano et al., 2010). To that end, the recently approved ROCK inhibitor netarsudil (Serle et al., 2018) directly targets the stiffened HTM to increase AH outflow via cell/tissue relaxation through reduction of actomyosin contractile tone (Rao et al., 2001, 2017; Tanna and Johnson, 2018; Wang and Chang, 2014; Zhang et al., 2012). And while not without merit, current HTM model systems are hampered by their inability to reliably and efficiently determine the relative contributions of HTM cells and their ECM to the onset and progression of glaucomatous HTM stiffening. No *in vitro* study to date has reported changes in tissue-level construct stiffness with DEX challenge/Y27632 rescue. To assess the utility of our HTM hydrogel as glaucoma disease model, we used proven corticosteroid induction of POAG-like conditions with DEX, and assessed the effects of ROCK inhibition with Y27632 on cell cytoskeletal organization and tissue-level function dependent on HTM cell-ECM interactions using three different HTM cell strains.

Independent of the HTM cell strain used, we showed increased HTM hydrogel contraction with DEX treatment, which is opposite to what a previous study found using simple collagen type I hydrogels encapsulated with bovine TM cells (Duffy and O'Reilly, 2018), but consistent

with data obtained from perfusion-cultured HTM tissues challenged with DEX (Johnson et al., 1990; Johnson, 2006). Actin abundance and organization are thought to modulate intracellular force generation and cell contractility; our results showed that DEX induced elevated f-actin and αSMA abundance and rearrangement, which is consistent with observations made using porous scaffolds seeded with HTM cells (Torrejon et al., 2016b). This suggests that increased actin abundance could induce cell contractile force generation to condense HTM cells within the 3D hydrogel network resulting in overall increased construct contractility. HTM remodeling is critical for proper tissue function, driven by the reciprocity between HTM cells and their ECM. By the same token, pathologic ECM remodeling contributes to glaucomatous tissue dysfunction. We observed increased morphological ECM remodeling (i. e., condensed hydrogels with qualitatively decreased network spacing) with DEX treatment. Furthermore, increased fibronectin deposition induced by DEX was confirmed in our model, which has been reported to contribute to elevated outflow resistance in the HTM with POAG (Acott and Kelley, 2008). Observed differences of fibronectin deposition with DEX challenge/Y27632 rescue between HTM hydrogels made using different cell strains likely reflect both inherent donor-to-donor variability and differential adaptive responses to the pharmacological agents, with possible cellular feedback and crosstalk between stimulated signaling pathways. These finding are in agreement with glaucomatous pathology and have all been linked to progressive HTM tissue stiffening. Importantly, consistent with the reported reduction of actomyosin contraction in HTM tissue following ROCK inhibition (Rao et al., 2001, 2017; Tanna and Johnson, 2018; Wang and Chang, 2014), we showed that Y27632 co-treatment (simulating a prophylactic approach) and sequential treatment (simulating a therapeutic approach) potently rescued the DEX-induced pathologic changes in HTM hydrogel contractility, condensation, and ECM deposition/remodeling across multiple HTM cell strains. Using an alternate pair of pharmacological induction/rescue of glaucomatous conditions - transforming growth factor-β2 (a potent cytokine implicated in POAG pathology (Lutjen-Drecoll, 2005)) and latrunculin-b (an actin filament depolymerizing agent (Rasmussen et al., 2014)), we were able to validate the utility of our HTM hydrogel as glaucoma disease model (Supplemental Information and Suppl. Fig. S9).

Patients with POAG, the most common subtype of glaucoma, typically suffer from elevated IOP and experience increased HTM stiffness, which in turn can negatively affect IOP and HTM cell function in a feed-forward loop (Faralli et al., 2019; Last et al., 2011; Ramos et al., 2009; Stamer and Acott, 2012; Wang et al., 2017a). It is perhaps because of these observations that more studies in recent years have focused on the biomechanical properties of tissues within the conventional outflow pathway, and their dynamic changes in disease. HTM tissue stiffness has been determined directly and indirectly in several studies. In an early report, HTM stiffness was shown to be ~20-fold higher in glaucomatous vs. normal eyes by atomic force microscopy (AFM) (Last et al., 2011). Several limitations to this study, however, may have resulted in over-estimated differences in tissue elasticity. In a recent elegant study using a novel indirect approach (with AFM correlation), HTM stiffness was determined to be ~1.4-fold greater in glaucomatous HTM tissues vs. normal controls (Wang et al., 2017a, 2017b). The discrepancies in both absolute and relative stiffness values (i.e., normal vs. glaucomatous) between the two studies most likely stem from methodological differences. We here showed a ~1.5–1.7-fold increase in HTM hydrogel stiffness using two different HTM cell strains with DEX treatment vs. controls as measured by a common oscillatory rheology shear-strain sweep test to determine hydrogel viscoelastic properties, consistent with the reported glaucomatous HTM tissue behavior (Wang et al., 2017a, 2017b). Y27632 treatment had precisely opposite effects, and was shown to prevent or rescue the DEX-induced pathologic changes, resulting in HTM hydrogel softening independent of the donor cell strain used. This was in agreement with the HTM hydrogel contraction, cytoskeletal rearrangement, and ECM remodeling/deposition data

suggesting potent therapeutic potential of Y27632 in support of clinical netarsudil use.

To further validate our hydrogel system as a glaucoma disease model, we encapsulated glaucomatous HTM (GTM) cells for comparisons with normal HTM hydrogels - matched to the HTM cell strain nearest in donor age - in absence or presence of additional corticosteroid stimulation. GTM cells were derived from a donor eye categorized as high-risk POAG suspect (contralateral eye diagnosed with moderate stage POAG). With long-term use of Brimonidine, Dorzolamide-timolol and Latanoprost, IOP was moderately-controlled and did not exceed 19 mmHg; however, outflow facility measurements upon receipt of the donor eyes demonstrated a ~50% reduction in normal AH outflow facility indicative of TM tissue damage. GTM hydrogels in absence of DEX induction were significantly more contracted and stiffened vs. normal controls, and ROCK inhibition using Y27632 restored hydrogel stiffness to baseline levels. This suggests that upon hydrogel encapsulation, GTM cells possess "pathologic memory"; and mirror key glaucomatous behaviors of DEX-induced normal HTM cells within the 3D biopolymer network and respond to proven targeted pharmacological treatment, providing ultimate validation of our tissue-engineered HTM hydrogel. We acknowledge that a limitation to our system is the lack of flow. Ongoing work to integrate the HTM hydrogel, with addition of a Schlemm's canal endothelial cell layer, on a microfluidics platform for measurements of flow resistance under dynamic conditions is expected to further expand the utility of our hydrogel-based glaucoma disease model.

In sum, we have developed a novel *in vitro* biomimetic HTM hydrogel model that allows for detailed investigation of the 3D HTM cell-ECM interface under normal and simulated POAG conditions upon *in situ* corticosteroid induction, or preferably encapsulation of confirmed glaucomatous cells. Importantly, unlike other model systems, the HTM biopolymer hydrogel enables correlative analyses of HTM cell cytoskeletal organization with tissue-level functional changes - namely glaucomatous contractility and stiffening - contingent on HTM cell-ECM interactions. The bidirectional responsiveness of the HTM hydrogel model system to pathologic challenge and rescue suggests promising potential to serve as a screening platform for new POAG treatments with focus on HTM cell/tissue biomechanics.

Declaration of competing interest

The authors report no conflicts of interest.

and S.H designed all experiments, collected, analyzed, and interpreted the data. T.B. and A.K. assisted with HTM cell isolation, ELP expression/purification, PDMS-mold design/3D printing, and imaging. R.W.W., N. A., and W.D.S. provided study materials. H.L. and S.H. wrote the manuscript. All authors collected data and commented on and approved the final manuscript. P.S.G. and S.H. conceived and supervised the research. Competing interests: The authors declare no conflict of interest. Data and materials availability: All data needed to evaluate the conclusions in the paper are present in the paper and/or the Supplementary Materials. Additional data related to this paper may be requested from the authors.

Appendix A. Supplementary data

Supplementary data to this article can be found online at https://doi.org/10.1016/j.exer.2021.108472.

References

Abu-Hassan, D.W., Acott, T.S., Kelley, M.J., 2014. The trabecular meshwork: a basic review of form and function. J. Ocul. Biol. 2, 9.

Acott, T.S., Kelley, M.J., 2008. Extracellular matrix in the trabecular meshwork. Exp. Eye Res. 86, 543–561.

Amano, M., Nakayama, M., Kaibuchi, K., 2010. Rho-kinase/ROCK: a key regulator of the cytoskeleton and cell polarity. Cytoskeleton (Hoboken) 67, 545–554.

Beidoe, G., Mousa, S.A., 2012. Current primary open-angle glaucoma treatments and future directions. Clin. Ophthalmol. 6, 1699–1707.

Bhadriraju, K., Chen, C.S., 2002. Engineering cellular microenvironments to improve cell-based drug testing. Drug Discov. Today 7, 612–620.

Bouchemi, M., Roubeix, C., Kessal, K., Riancho, L., Raveu, A.L., Soualmia, H., Baudouin, C., Brignole-Baudouin, F., 2017. Effect of benzalkonium chloride on trabecular meshwork cells in a new in vitro 3D trabecular meshwork model for glaucoma. Toxicol. Vitro 41, 21–29.

Brubaker, R.F., 1991. Flow of aqueous humor in humans [The Friedenwald Lecture]. Invest. Ophthalmol. Vis. Sci. 32, 3145–3166.

Caliari, S.R., Burdick, J.A., 2016. A practical guide to hydrogels for cell culture. Nat. Methods 13, 405–414.

Daamen, W.F., Veerkamp, J.H., van Hest, J.C., van Kuppevelt, T.H., 2007. Elastin as a biomaterial for tissue engineering. Biomaterials 28, 4378–4398.

Dasso, L., Al-Khaled, T., Sonty, S., Aref, A.A., 2018. Profile of netarsudil ophthalmic solution and its potential in the treatment of open-angle glaucoma: evidence to date. Clin. Ophthalmol. 12, 1939–1944.

Dautriche, C.N., Szymanski, D., Kerr, M., Torrejon, K.Y., Bergkvist, M., Xie, Y., Danias, J., Stamer, W.D., Sharfstein, S.T., 2015. A biomimetic Schlemm's canal inner wall: a model to study outflow physiology, glaucoma pathology and high-throughput drug screening. Biomaterials 65, 86–92.

Dismuke, W.M., Liang, J., Overby, D.R., Stamer, W.D., 2014. Concentration-related effects of nitric oxide and endothelin-1 on human trabecular meshwork cell contractility. Exp. Eye Res. 120, 28–35.

Duffy, L., O'Reilly, S., 2018. Functional implications of cross-linked actin networks in trabecular meshwork cells. Cell. Physiol. Biochem. 45, 783–794.

Edmondson, R., Broglie, J.J., Adcock, A.F., Yang, L., 2014. Three-dimensional cell culture systems and their applications in drug discovery and cell-based biosensors. Assay Drug Dev. Technol. 12, 207–218.

Fan, B.J., Wang, D.Y., Tham, C.C.Y., Lam, D.S.C., Pang, C.P., 2008. Gene expression profiles of human trabecular meshwork cells induced by triamcinolone and dexamethasone. Invest. Ophthalmol. Vis. Sci. 49, 1886–1897.

Faralli, J.A., Filla, M.S., Peters, D.M., 2019. Role of fibronectin in primary open angle glaucoma. Cells 8 (12), 1518.

Frantz, C., Stewart, K.M., Weaver, V.M., 2010. The extracellular matrix at a glance. J. Cell Sci. 123, 4195–4200.

Gerometta, R., Podos, S.M., Candia, O.A., Wu, B., Malgor, L.A., Mittag, T., Danias, J., 2004. Steroid-induced ocular hypertension in normal cattle. Arch. Ophthalmol. 122, 1492–1497.

Gould, D.B., John, S.W.M., 2002. Anterior segment dysgenesis and the developmental glaucomas are complex traits. Hum. Mol. Genet. 11, 1185–1193.

Green, J.J., Elisseeff, J.H., 2016. Mimicking biological functionality with polymers for biomedical applications. Nature 540, 386–394.

Hann, C.R., Fautsch, M.P., 2011. The elastin fiber system between and adjacent to collector channels in the human juxtacanalicular tissue. Invest. Ophthalmol. Vis. Sci. 52, 45–50.

Johnson, D.H., Bradley, J.M., Acott, T.S., 1990. The effect of dexamethasone on glycosaminoglycans of human trabecular meshwork in perfusion organ culture. Invest. Ophthalmol. Vis. Sci. 31, 2568–2571.

Johnson, M., 2006. `What controls aqueous humour outflow resistance? Exp. Eye Res. 82, 545–557.

Keller, K.E., Acott, T.S., 2013. The juxtacanalicular region of ocular trabecular meshwork: a tissue with a unique extracellular matrix and specialized function. J. Ocul. Biol. 1, 3.

Keller, K.E., Bhattacharya, S.K., Borras, T., Brunner, T.M., Chansangpetch, S., Clark, A.F., Dismuke, W.M., Du, Y., Elliott, M.H., Ethier, C.R., Faralli, J.A., Freddo, T.F., Fuchshofer, R., Giovingo, M., Gong, H., Gonzalez, P., Huang, A., Johnstone, M.A., Kaufman, P.L., Kelley, M.J., Knepper, P.A., Kopczynski, C.C., Kuchtey, J.G., Kuchtey, R.W., Kuehn, M.H., Lieberman, R.L., Lin, S.C., Liton, P., Liu, Y., Lutjen-Drecoll, E., Mao, W., Masis-Solano, M., McDonnell, F., McDowell, C.M., Overby, D. R., Pattabiraman, P.P., Raghunathan, V.K., Rao, P.V., Rhee, D.J., Chowdhury, U.R., Russell, P., Samples, J.R., Schwartz, D., Stubbs, E.B., Tamm, E.R., Tan, J.C., Toris, C. B., Torrejon, K.Y., Vranka, J.A., Wirtz, M.K., Yorio, T., Zhang, J., Zode, G.S., Fautsch, M.P., Peters, D.M., Acott, T.S., Stamer, W.D., 2018. Consensus recommendations for trabecular meshwork cell isolation, characterization and culture. Exp. Eye Res. 171, 164–173.

Kelley, M.J., Rose, A.Y., Keller, K.E., Hessle, H., Samples, J.R., Acott, T.S., 2009. Stem cells in the trabecular meshwork: present and future promises. Exp. Eye Res. 88, 747–751.

Khademhosseini, A., Langer, R., 2007. Microengineered hydrogels for tissue engineering. Biomaterials 28, 5087–5092.

Koga, T., Koga, T., Awai, M., Tsutsui, J., Yue, B.Y., Tanihara, H., 2006. Rho-associated protein kinase inhibitor, Y-27632, induces alterations in adhesion, contraction and motility in cultured human trabecular meshwork cells. Exp. Eye Res. 82, 362–370.

Kwon, Y.H., Fingert, J.H., Kuehn, M.H., Alward, W.L., 2009. Primary open-angle glaucoma. N. Engl. J. Med. 360, 1113–1124.

Lampi, M.C., Reinhart-King, C.A., 2018. Targeting extracellular matrix stiffness to attenuate disease: from molecular mechanisms to clinical trials. Sci. Transl. Med. 10, eaao0475.

Langer, R., Vacanti, J.P., 1993. Tissue engineering. Science 260, 920–926.

Last, J.A., Pan, T., Ding, Y., Reilly, C.M., Keller, K., Acott, T.S., Fautsch, M.P., Murphy, C. J., Russell, P., 2011. Elastic modulus determination of normal and glaucomatous human trabecular meshwork. Invest. Ophthalmol. Vis. Sci. 52, 2147–2152.

Lee, K.Y., Mooney, D.J., 2001. Hydrogels for tissue engineering. Chem. Rev. 101, 1869–1879.

Leung, T., Manser, E., Tan, L., Lim, L., 1995. A novel serine/threonine kinase binding the Ras-related RhoA GTPase which translocates the kinase to peripheral membranes. J. Biol. Chem. 270, 29051–29054.

Lin, C.W., Sherman, B., Moore, L.A., Laethem, C.L., Lu, D.W., Pattabiraman, P.P., Rao, P. V., deLong, M.A., Kopczynski, C.C., 2018. Discovery and preclinical development of netarsudil, a novel ocular hypotensive agent for the treatment of glaucoma. J. Ocul. Pharmacol. Therapeut. 34, 40–51.

Lutjen-Drecoll, E., 2005. Morphological changes in glaucomatous eyes and the role of TGFbeta2 for the pathogenesis of the disease. Exp. Eye Res. 81, 1–4.

Mazzocchi, A., Devarasetty, M., Herberg, S., Petty, W.J., Marini, F., Miller, L., Kucera, G., Dukes, D.K., Ruiz, J., Skardal, A., Soker, S., 2019. Pleural effusion aspirate for use in 3D lung cancer modeling and chemotherapy screening. ACS Biomater. Sci. Eng. 5, 1937–1943.

Mithieux, S.M., Weiss, A.S., 2005. Elastin. Adv. Protein Chem. 70, 437–461.

Nettles, D.L., Chilkoti, A., Setton, L.A., 2010. Applications of elastin-like polypeptides in tissue engineering. Adv. Drug Deliv. Rev. 62, 1479–1485.

Osmond, M., Bernier, S.M., Pantcheva, M.B., Krebs, M.D., 2017. Collagen and collagen-chondroitin sulfate scaffolds with uniaxially aligned pores for the biomimetic, three dimensional culture of trabecular meshwork cells. Biotechnol. Bioeng. 114, 915–923.

Osmond, M.J., Krebs, M.D., Pantcheva, M.B., 2020. Human trabecular meshwork cell behavior is influenced by collagen scaffold pore architecture and glycosaminoglycan composition. Biotechnol. Bioeng. 17 (10), 3150–3159.

Overby, D.R., Clark, A.F., 2015. Animal models of glucocorticoid-induced glaucoma. Exp. Eye Res. 141, 15–22.

Paylakhi, S.H., Yazdani, S., April, C., Fan, J.-B., Moazzeni, H., Ronaghi, M., Elahi, E., 2012. Non-housekeeping genes expressed in human trabecular meshwork cell cultures. Mol. Vis. 18, 241–254.

Quigley, H.A., 1993. Open-angle glaucoma. N. Engl. J. Med. 328, 1097–1106.

Quigley, H.A., Broman, A.T., 2006. The number of people with glaucoma worldwide in 2010 and 2020. Br. J. Ophthalmol. 90, 262–267.

Ramos, R.F., Sumida, G.M., Stamer, W.D., 2009. Cyclic mechanical stress and trabecular meshwork cell contractility. Invest. Ophthalmol. Vis. Sci. 50, 3826–3832.

Rao, P.V., Deng, P.F., Kumar, J., Epstein, D.L., 2001. Modulation of aqueous humor outflow facility by the Rho kinase-specific inhibitor Y-27632. Invest. Ophthalmol. Vis. Sci. 42, 1029–1037.

Rao, P.V., Pattabiraman, P.P., Kopczynski, C., 2017. Role of the Rho GTPase/Rho kinase signaling pathway in pathogenesis and treatment of glaucoma: bench to bedside research. Exp. Eye Res. 158, 23–32.

Rasmussen, C.A., Kaufman, P.L., Ritch, R., Haque, R., Brazzell, R.K., Vittitow, J.L., 2014. Latrunculin B reduces intraocular pressure in human ocular hypertension and primary open-angle glaucoma. Transl Vis Sci Technol 3, 1.

Riento, K., Ridley, A.J., 2003. ROCKs: multifunctional kinases in cell behaviour. Nat. Rev. Mol. Cell Biol. 4, 446–456.

Rybkin, I., Gerometta, R., Fridman, G., Candia, O., Danias, J., 2017. Model systems for the study of steroid-induced IOP elevation. Exp. Eye Res. 158, 51–58.

Saccà, S.C., Tirendi, S., Scarfì, S., Passalacqua, M., Oddone, F., Traverso, C.E., Vernazza, S., Bassi, A.M., 2020. An advanced in vitro model to assess glaucoma onset. ALTEX - Alternatives to animal experimentation 37 (2), 265–274.

Schmittgen, T.D., Livak, K.J., 2008. Analyzing real-time PCR data by the comparative C (T) method. Nat. Protoc. 3, 1101–1108.

Seliktar, D., 2012. Designing cell-compatible hydrogels for biomedical applications. Science 336, 1124–1128.

Serle, J.B., Katz, L.J., McLaurin, E., Heah, T., Ramirez-Davis, N., Usner, D.W., Novack, G. D., Kopczynski, C.C., 2018. Two phase 3 clinical trials comparing the safety and

efficacy of netarsudil to timolol in patients with elevated intraocular pressure: rho kinase elevated IOP treatment trial 1 and 2 (ROCKET-1 and ROCKET-2). Am. J. Ophthalmol. 186, 116–127.

Shirzaei Sani, E., Portillo-Lara, R., Spencer, A., Yu, W., Geilich, B.M., Noshadi, I., Webster, T.J., Annabi, N., 2018. Engineering adhesive and antimicrobial hyaluronic acid/elastin-like polypeptide hybrid hydrogels for tissue engineering applications. ACS Biomater. Sci. Eng. 4, 2528–2540.

Siegner, A., May, C.A., Welge-Lüssen, U.W., Bloemendal, H., Lütjen-Drecoll, E., 1996. Alpha B-crystallin in the primate ciliary muscle and trabecular meshwork. Eur. J. Cell Biol. 71, 165–169.

Stamer, W.D., Acott, T.S., 2012. Current understanding of conventional outflow dysfunction in glaucoma. Curr. Opin. Ophthalmol. 23, 135–143.

Stamer, W.D., Clark, A.F., 2017. The many faces of the trabecular meshwork cell. Exp. Eye Res. 158, 112–123.

Stamer, W.D., Roberts, B.C., Howell, D.N., Epstein, D.L., 1998. Isolation, culture, and characterization of endothelial cells from Schlemm's canal. Invest. Ophthalmol. Vis. Sci. 39, 1804–1812.

Stamer, W.D., Seftor, R.E., Williams, S.K., Samaha, H.A., Snyder, R.W., 1995. Isolation and culture of human trabecular meshwork cells by extracellular matrix digestion. Curr. Eye Res. 14, 611–617.

Stamer, W.D., Williams, A.M., Pflugfelder, S., Coupland, S.E., 2018. Accessibility to and quality of human eye tissue for research: a cross-sectional survey of ARVO members. Invest. Ophthalmol. Vis. Sci. 59, 4783–4792.

Svitkina, T., 2018. The actin cytoskeleton and actin-based motility. Cold Spring Harb Perspect Biol 10, a018267.

Tamm, E.R., 2009. The trabecular meshwork outflow pathways: structural and functional aspects. Exp. Eye Res. 88, 648–655.

Tamm, E.R., Braunger, B.M., Fuchshofer, R., 2015. Intraocular pressure and the mechanisms involved in resistance of the aqueous humor flow in the trabecular meshwork outflow pathways. Prog. Mol. Biol. Transl. Sci. 134, 301–314.

Tanna, A.P., Esfandiari, H., Teramoto, K., 2020. Reversible corneal endothelial abnormalities with netarsudil. J. Glaucoma 29 (6), e41–e43.

Tanna, A.P., Johnson, M., 2018. Rho kinase inhibitors as a novel treatment for glaucoma and ocular hypertension. Ophthalmology 125, 1741–1756.

Tektas, O.-Y., Lütjen-Drecoll, E., 2009. Structural changes of the trabecular meshwork in different kinds of glaucoma. Exp. Eye Res. 88, 769–775.

Tham, Y.C., Li, X., Wong, T.Y., Quigley, H.A., Aung, T., Cheng, C.Y., 2014. Global prevalence of glaucoma and projections of glaucoma burden through 2040: a systematic review and meta-analysis. Ophthalmology 121, 2081–2090.

Tirella, A., Liberto, T., Ahluwalia, A., 2012. Riboflavin and collagen: new crosslinking methods to tailor the stiffness of hydrogels. Mater. Lett. 74, 58–61.

Torrejon, K.Y., Papke, E.L., Halman, J.R., Bergkvist, M., Danias, J., Sharfstein, S.T., Xie, Y., 2016a. TGFβ2-induced outflow alterations in a bioengineered trabecular meshwork are offset by a rho-associated kinase inhibitor. Sci. Rep. 6, 38319.

Torrejon, K.Y., Papke, E.L., Halman, J.R., Stolwijk, J., Dautriche, C.N., Bergkvist, M., Danias, J., Sharfstein, S.T., Xie, Y., 2016b. Bioengineered glaucomatous 3D human trabecular meshwork as an in vitro disease model. Biotechnol. Bioeng. 113, 1357–1368.

Torrejon, K.Y., Pu, D., Bergkvist, M., Danias, J., Sharfstein, S.T., Xie, Y., 2013. Recreating a human trabecular meshwork outflow system on microfabricated porous structures. Biotechnol. Bioeng. 110, 3205–3218.

van Oosten, A.S.G., Chen, X., Chin, L., Cruz, K., Patteson, A.E., Pogoda, K., Shenoy, V.B., Janmey, P.A., 2019. Emergence of tissue-like mechanics from fibrous networks confined by close-packed cells. Nature 573, 96–101.

Vernazza, S., Tirendi, S., Scarfì, S., Passalacqua, M., Oddone, F., Traverso, C.E., Rizzato, I., Bassi, A.M., Sacca, S.C., 2019. 2D- and 3D-cultures of human trabecular meshwork cells: a preliminary assessment of an in vitro model for glaucoma study. PloS One 14, e0221942.

Waduthanthri, K.D., He, Y., Montemagno, C., Cetinel, S., 2019. An injectable peptide hydrogel for reconstruction of the human trabecular meshwork. Acta Biomater. 100, 244–254.

Wang, K., Johnstone, M.A., Xin, C., Song, S., Padilla, S., Vranka, J.A., Acott, T.S., Zhou, K., Schwaner, S.A., Wang, R.K., Sulchek, T., Ethier, C.R., 2017a. Estimating human trabecular meshwork stiffness by numerical modeling and advanced OCT imaging. Invest. Ophthalmol. Vis. Sci. 58, 4809–4817.

Wang, K., Read, A.T., Sulchek, T., Ethier, C.R., 2017b. Trabecular meshwork stiffness in glaucoma. Exp. Eye Res. 158, 3–12.

Wang, S.K., Chang, R.T., 2014. An emerging treatment option for glaucoma: rho kinase inhibitors. Clin. Ophthalmol. 8, 883–890.

Wisely, C.E., Liu, K.C., Gupta, D., Carlson, A.N., Asrani, S.G., Kim, T., 2020. Reticular bullous epithelial edema in corneas treated with netarsudil: a case Series. Am. J. Ophthalmol. 217, 20–26.

Zhang, K., Zhang, L., Weinreb, R.N., 2012. Ophthalmic drug discovery: novel targets and mechanisms for retinal diseases and glaucoma. Nat. Rev. Drug Discov. 11, 541–559.

Zhang, Y.N., Avery, R.K., Vallmajo-Martin, Q., Assmann, A., Vegh, A., Memic, A., Olsen, B.D., Annabi, N., Khademhosseini, A., 2015. A highly elastic and rapidly crosslinkable elastin-like polypeptide-based hydrogel for biomedical applications. Adv. Funct. Mater. 25, 4814–4826.

Zhang, Y.S., Khademhosseini, A., 2017. Advances in engineering hydrogels. Science 356, eaaf3627.